STAR-RIS-Enabled Secure Dual-Functional Radar-Communications: Joint Waveform and Reflective Beamforming Optimization

Chao Wang, *Senior Member, IEEE*, Cheng-Cai Wang, Zan Li, *Senior Member, IEEE*, Derrick Wing Kwan Ng, *Fellow, IEEE*, Kai-Kit Wong, *Fellow, IEEE*, Naofal Al-Dhahir, *Fellow, IEEE*, and Dusit Niyato, *Fellow, IEEE*

***Abstract*—Considering a simultaneously transmitting and reflecting reconfigurable intelligent surfaces (STAR-RIS)-aided dual-functional radar-communications (DFRC) system, this paper proposes a symbol-level precoding-based scheme for concurrent securing confidential information transmission and performing target sensing, where the public signals intended for multiple unclassified users are exploited to deceive the multiple potential malicious radar targets. Specifically, the STAR-RIS-aided DFRC system design is formulated as a joint optimization problem that determines the transmission waveform signal, the transmission and reflection coefficients of STAR-RIS. The objective is to maximize the average received radar sensing power subject to the quality-of-service constraints for multiple communication users, the security constraint for multiple potential eavesdroppers, as well as various practical waveform design restrictions. However, the formulated problem is challenging to handle due to its nonconvexity. Furthermore, the high dimensionality of the optimization variables also renders existing optimization algorithms inefficient. To address these issues, we propose a distance-majorization induced low-complexity algorithm to obtain an efficient solution, which converts the nonconvex joint design problem into a sequence of subproblems that can be solved in closed-form, relieving the required high computational burden of the conventional approaches, e.g., the interior point method. Simulation results confirm the effectiveness of the STAR-RIS in improving the DFRC performance. Besides, by comparing with the state-of-the-art alternating direction method of multipliers (ADMM) algorithm, simulation results validate the efficiency of our proposed optimization algorithm and show that it enjoys excellent scalability for different number of T-R elements equipped at the STAR-RIS.**

***Index Terms*—STAR-RIS, dual-functional radar-communication, symbol-level precoding, distance-majorization.**

Part of this work has been presented at the IEEE International Conference on Communications Workshops (ICCW' 2023) [1]

This work of C. Wang was supported in part by the National Natural Science Foundation of China under Grants 61801518, in part by the Key Research and Development Program of Shaanxi (ProgramNo. 2022KW-03), in part by the Defense Industrial Technology Development Program under Grant JCKY2021608B001, JCKY2021608B001, JCKY2021110B143, and JCKY2020204B027, in part by the Fundamental Research Funds for the Central Universities under Grant ZYTS23177, in part by the China Postdoctoral Science Foundation under Grant 2020M683428. The work of C. C. Wang is supported by Beijing Nova Program. The work of Z. Li was supported by the National Science Fund for Distinguished Young Scholars of China under Grant 61825104. The work of D. W. K. Ng is supported by the Australian Research Council's Discovery Project (DP210102169). The work of K. K. Wong is supported in part by the Engineering and Physical Sciences Research Council (EPSRC) under grant EP/V052942/1. The work of N. Al-Dhahir was supported by Erik Jonsson distinguished Professorship at UT-Dallas. The work of D. Niyato was supported by the National Research Foundation, Singapore, and Infocomm Media Development Authority under its Future Communications Research & Development Programme, DSO National Laboratories under the AI Singapore Programme (AISG Award No: AISG2-RP-2020-019), Energy Research Test-Bed and Industry Partnership Funding Initiative, Energy Grid (EG) 2.0 programme, DesCartes and the Campus for Research Excellence and Technological Enterprise (CREATE) programme, and MOE Tier 1 (RG87/22). (*Corresponding authors: Chao Wang and Cheng-Cai Wang.*)

C. Wang and Z. Li are both with the Integrated Service Networks Lab, Xidian University, Xi'an 710071, China.(e-mail: drchaowang@126.com).

C. C. Wang is with the School of Automation Science and Electrical Engineering, Beihang University, Beijing 100191, China (e-mail: ccwang@pku.edu.cn).

D. W. K. Ng is with the School of Electrical Engineering and Telecommunications, University of New South Wales, Sydney, 2052, Australia (w.k.ng@unsw.edu.au).

K.-K. Wong is with the Department of Electronic and Electrical Engineering, University College London, London WC1E 6BT, U.K. (e-mail: kai-kit.wong@ucl.ac.uk).

N. Al-Dhahir is with the Department of Electrical and Computer Engineering, the University of Texas at Dallas, Richardson, TX 75080 USA (e-mail: aldhahir@utdallas.edu).

D. Niyato is with Nanyang Technological University, Singapore 639798 (e-mail: dniyato@ntu.edu.sg).

I. Introduction

The upcoming sixth-generation (6G) networks will enable a plethora of emerging applications such as autonomous driving, smart factories, intruder detection, and localization tracking to name a few [2]. Hence, there is an urgent need to integrate radar sensing capability into the next-generation wireless networks to establish perceptive mobile networks via the notion of dual-functional radar-communications (DFRC) [3]. In fact, traditional wireless communications and radar sensing have developed independently in the past decades due to their inherently different functionalities. The initial study on DFRC can be traced back to the 1960s, where pulse code groups were adopted for tracking space vehicles while performing information transmission [4]. However, the research on DFRC did not receive significant attention until the 2010s. In recent years, the deficiency of spectral resources and the increasing demand for perceptive mobile networks have triggered the need for efficient DFRC designs to achieve satisfactory communication and sensing performance simultaneously [5]–[7]. In general, there are two main research trends on DFRC, radar-centric and communication-centric system designs [8], respectively. Specifically, radar-centric designs exploit radar probing signals as the information carrier that modulates communication data on the radar pulses by adopting interpulse modulation or intrapulse modulation [9], [10]. However, existing radar surveillance systems are mainly designed for military applications. Therefore, modifying those systems for granting additional DFRC functionality may not be allowed due to strict military security requirements [11].

On the other hand, communication-centric systems adopt communication waveforms to perform radar sensing, where the object information can be extracted from the received echo signals [11]–[13]. Since a cellular base station (BS) offers commercial communication services, compared with dedicated military-based radar systems, it is relatively free of bureaucracy in modifying or upgrading the BSs for integrating the radar sensing functionality into existing wireless networks [7]. Along this line, the works of [14], [15] studied the joint transceiver design for the coexistence of multiple-input multiple-output (MIMO) radar and MIMO communications in realizing the DFRC functionality. Furthermore, by fixing the transmit covariances of DFRC signals, the work in [12] investigated the joint design of the precoders for radar sensing and communications to maximize the minimum received signal-to-interference-plus-noise ratio (SINR) at multiple communication users. Besides, the works in [16], [17] adopted different advanced multiple access techniques to establish different joint radar and multiuser communication frameworks. However, the aforementioned works, e.g., [12], [16], [17] investigated only block-level precoding techniques for designing an invariant precoder for a coherence time block over multiple data symbols, which can only guarantee the statistical performance of radar sensing. However, in various wireless applications where only a small number of echo signals can be collected, the radar sensing performance is generally degraded [11]. To this end, the works of [11], [18] employed the symbol-level precoding technique to study the instantaneous signal design for minimizing the squared error between the instantaneous transmit beam pattern and the desired pattern such that efficient sensing can be performed in each time slot. Yet, introducing additional radar functionalities to communication networks would inevitably degrade the communication performance as the two desired goals may conflict with each other. As a result, there is an urgent need for novel technologies that can establish a symbiotic DFRC system to achieve both signal broadcasting and radar sensing efficiently.

On the other hand, it is well known that reconfigurable intelligent surfaces (RIS) can customize wireless channels to facilitate efficient communications through optimized signal reflection which has been regarded as a promising technology to enable the future 6G era [19]–[21]. Inspired by the great potential brought by RIS, numerous studies have been devoted to the investigation of the RIS-aided DFRC system design in recent years [22]–[26]. For instance, the work of [24] exploited the RIS potential to improve the performance of DFRC systems and proposed a joint design of the transmit signal waveform and passive beamforming to maximize the radar output SINR subject to the quality-of-service (QoS) communication constraints. Besides, the work of [27] proposed an RIS-aided covert communciations and radar sensing system for effective target detection and covert communications. Nevertheless, the traditional RIS can only reflect the incident signals on the reflecting side of the surface which provides limited service coverage with only 180^o field-of-view [28]. Recently, to address the aforementioned disadvantages, STAR-RIS has been proposed in [29]–[31], whose elements can enable both signal transmission and reflection [32]. Different from RIS, STAR-RIS can extend the service coverage from the half-space to the full-space achieving 360^o coverage through transmitting and reflecting the impinging signals simultaneously [33]. Therefore, the benefit of STAR-RIS over RIS is to enlarge the signal coverage and increase the application flexibility [32]. In fact, a telecommunication company DOCOMO has conducted a trial of the world's first prototype of STAR-RIS successfully and demonstrated its great potential [34]. Thanks to its various potentials, STAR-RIS-aided communications have received increasing attentions. In particular, the authors in [35] studied the performance of STAR-RIS-aided non-orthogonal multiple access. Recently, some works such as [36], have studied the STAR-RIS-aided DFRC. Despite the various attempts have made, the research in this emerging area is still in infancy.

Moreover, compared with radar systems, communication-centric DFRC systems encounter serious security problems, since communication signals enabled radar sensing are generally susceptible to potential eavesdropping attacks due to the reuse of information-carrying signal waveform [37]–[39]. Considering that the malicious target acts as an eavesdropper (Eve) endangering the communication security, the work of [37] proposed to employ the artificial noise technique to secure a DFRC system against malicious potential eavesdropping. Unfortunately, the application of additional artificial noise would inevitably increase the interference and deteriorate the network performance. Hence, the authors of [38] employed the symbol-level precoding technique to design the signal waveform for exploiting the inherent multiuser interference to further secure DFRC systems. Compared with DFRC, the security threat in STAR-RIS aided DFRC is more severe due to the extra strong path introduced by STAR-RIS to the malicious radar targets. Besides, the precoder optimization of STAR-RIS aided DFRC is nonconvex. Specifically, the nonconvex radar waveform constraints have made convex optimization algorithms not applicable. More importantly, the high-dimensionality of the optimization variables introduced by STAR-RIS makes existing approximate optimization approach, e.g., semidefinite relaxation (SDR)-based algorithm, inefficient for handling the joint design optimization problem. To the best of our knowledge, physical layer security (PLS) scheme for STAR-RIS-aided DFRC has not been considered before.

Against this background, this work investigates the PLS of STAR-RIS-aided DFRC. Specifically, considering that multiple malicious targets may potentially eavesdrop the confidential information intended to the secure user, we adopt the symbol-level precoding technique to design an efficient deception strategy for securing DFRC. Moreover, compared with the conference paper [1] which only sketches the algorithm, this article details its derivations. Furthermore, this article also shows its convergence performance and computational complexity. Our contributions can be summarized as follows:

1) We investigate the joint optimization of the signal waveform, the active beamforming at the BS, the passive transmit and reflective beamforming at the STAR-RIS to exploit the multiuser interference for maximizing the radar sensing power of DFRC while guaranteeing the

communication reliability and security. In particular, the superimposed signal received at each communication user is focused on the "constructive region" of its desired information symbols, which can improve the signal reception quality at the communication users. In contrast, the superimposed signals received at the multiple malicious radar targets are designed to fall in the "constructive region" of the unclassified information symbols intended for the public users. Hence, multiple malicious radar targets are deceived in believing that the unclassified information symbols are the desired confidential ones, which protects the confidential information intending to the secure user from potential eavesdropping.

2) The formulated joint optimization problem is nonconvex due to the coupling among optimization variables and nonconvex constraints. Besides, the existing symbol-level precoding techniques increase the dimensionality of the optimization variables significantly such that solving the joint optimization problem is computationally intensive. To address these issues, we propose a low-complexity distance-majorization-based iterative algorithm. Specifically, we convert the considered nonconvex joint optimization problem into a sequence of subproblems that can be solved in a closed-form. Therefore, the proposed approach enjoys a significant reduction of computational complexity in solving the high-dimensional optimization problem, compared with traditional optimization algorithms adopting the interior-point algorithm.
3) Simulation results show that our proposed joint optimization algorithm can achieve better performance than the ADMM-based benchmark algorithm. Furthermore, the potential of STAR-RIS for improving the DFRC performance has been validated and the performance improvement enlarges with the increasing power budget of the BS.

Notation: χ_k^2 denotes a central chi-squared random variable with k DoF. $\mathcal{R}(a)$ and $\mathcal{I}(a)$ denotes the real and imaginary part of a complex number a. $(\cdot)^T$, $(\cdot)^H$, and $||\cdot||_2$ denote the transpose, the conjugate transpose, and the L_2 norm, respectively; $\mathrm{vec}(\cdot)$, $\mathrm{Tr}(\cdot)$ and $(\cdot)^{-1}$ denote the vectorization, trace and inverse of an input matrix, respectively; $\ln(\cdot)$ denotes the natural logarithm; $\mathbf{x} \sim \mathcal{CN}(\mathbf{\Lambda}, \mathbf{\Delta})$ denotes the complex Gaussian vector $\mathbf{x}$ with mean vector $\mathbf{\Lambda}$ and covariance matrix $\mathbf{\Delta}$. $\mathbf{I}_N$ is the $N \times N$ identity matrix. $\otimes$ denotes the Kronecker product. $\mathrm{diag}(\cdot)$ denotes a diagonal matrix. $\mathrm{dist}^2(\mathbf{x}, \mathbf{C}) \triangleq \inf_{\mathbf{y}\in\mathbf{C}} ||\mathbf{x}-\mathbf{y}||^2$ is the minimum squared Euclidean distance from vector $\mathbf{x}$ to the set $\mathbf{C}$. $\mathcal{O}(\cdot)$ is the big-O notation.

II. System Model and Performance Metric

A. System Model

We consider a STAR-RIS-enabled DFRC system as illustrated in Fig. 1, where a multi-antenna dual-functional BS serves K_u downlink single-antenna users while detecting K_e point-like targets with the help of a STAR-RIS. The BS is equipped with N_t transmitting antennas where $N_t \geq K_u$. Besides, the information intended to the secure user is confidential while the information transmitted to the remaining users

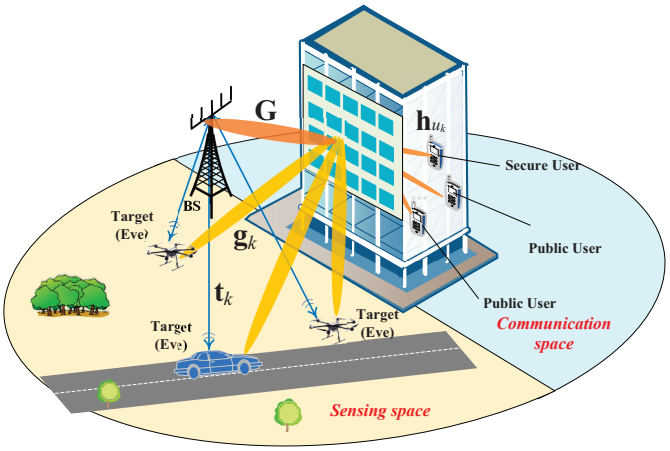

Fig. 1. An illustration of the considered STARS-aided DFRC system.

is public[1]. Similar to [40]–[42], we assume that the STAR-RIS is equipped with a uniform linear array (ULA) consisting of a total of N T-R elements. Also, the direct channel from the BS to the users are blocked due to the obstacles and the indirect channel is established through the signal reflection at the STAR-RIS. In particular, the BS firstly broadcasts the information signals to the users while illuminating the targets of interest. Then, the BS estimates the parameters of the targets by exploiting the echo signals received from the targets. Since adopting conventional communication signals to detect targets requires only minimal modifications to existing wireless communication systems and does not introduce extra network interference. As such, following [11], [14], [18], [43], we only employ communication signals to realize DFRC systems. However, considering that multiple spatially separated malicious targets may also act as eavesdroppers (Eves) to wiretap the confidential information intended to the secure user, we follow [37], [38] to assume that each malicious target is a single-antenna Eve which potentially wiretaps the confidential information independently[2].

In this work, we propose to adopt the symbol-level precoding technique to perform signal broadcasting and radar sensing simultaneously. In particular, the transmitted signals in the lth time slot are the non-linear mapping from the information symbols intended for the K_u users, $\mathbf{x}[l] \triangleq [x_1[l], \ldots, x_{K_u}[l]]^T$ to the baseband signal transmitted from the N_t antennas, $\mathbf{s}[l] \triangleq [s_1[l], \ldots, s_{N_t}[l]]^T$. Different from the block-level precoding techniques that adopt the second-order statistics of the signals, e.g., the covariance matrix, to design the signal transmission [12], [14], [16], [44], the symbol-level precoding optimizes the instantaneous signal $\mathbf{s}[l]$ directly [11], [18], which offers more degrees-of-freedom (DoF) for the DFRC system design to improve the performance.

This work concentrates on studying the joint optimization of the transmission signal $\mathbf{s}[l]$, the matrices of the trans-

[1]To simplify the presentation, we consider only a single secure user. Note that the proposed secure transmission scheme can be extended to the case of multiple confidential users directly at the expense of more involved notations.

[2]Multiple malicious radar targets are assumed to wiretap the confidential information in a non-cooperative manner since multiple targets are spatially separated and collaborative eavesdropping is challenging to carry out.

mission coefficients and reflection coefficients at the STAR-RIS, i.e., $\mathbf{\Theta}_t \triangleq \text{diag}\left(\tau_{t,1}e^{j\theta_{t,1}}, \ldots, \tau_{t,N}e^{j\theta_{t,N}}\right)$ and $\mathbf{\Theta}_r \triangleq \text{diag}\left(\tau_{r,1}e^{j\theta_{r,1}}, \ldots, \tau_{r,N}e^{j\theta_{r,N}}\right)$, respectively, where $\tau_{t,i}$ and $0 \leq \theta_{t,i} \leq 2\pi$ are the amplitude and phase of the ith transmission coefficient, respectively. Besides, $\tau_{r,i}$ and $\theta_{r,i}$ are the amplitude and phase of the ith reflection coefficient, respectively. Following the existing works on DFRC, e.g., [22], [45], [46], the joint design is formulated as an optimization problem that maximizes the total illumination power along the target directions taking into account the constructive interference (CI)-type constraints on the communication users, security constraints on the secure user, and other practical constraints on the transmit beampatterns including the peak-to-average-power ratio and similarity constraints [47].

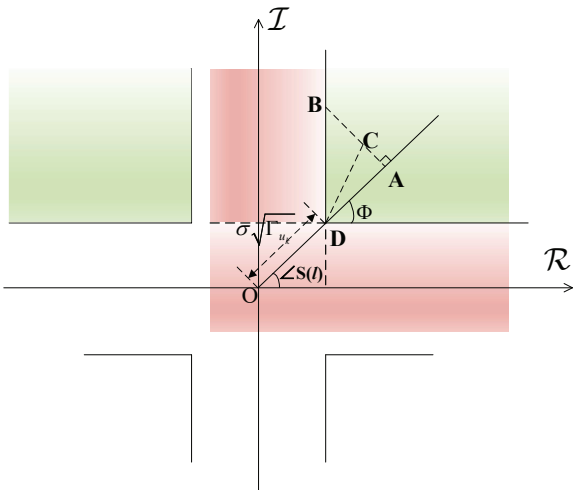

Fig. 2. Illustration of the constructive interference using QPSK as an example, where the green and red shaded regions represent the constructive and destructive regions.

B. Multiuser Communications Performance Metric

To simplify the presentation, like [11], [24], the data symbols are assumed to be modulated using the phase-shift-keying (PSK) scheme. Besides, following [36], the whole service area is assumed to be divided into two half-spaces, namely communication space and sensing space, respectively, where multiple communication users in the communication space are served by $\mathbf{\Theta}_t$ and multiple malicious targets in the sensing space are served by $\mathbf{\Theta}_r$. Then, at the lth time slot, the symbol-level precoded signal vector is $\mathbf{s}[l]$ and the received signal at the kth user is given by

$$y_{u_k}[l] = \mathbf{h}_{u_k}^H \mathbf{\Theta}_t \mathbf{G}\mathbf{S}(:,l) + n_{u_k}[l],\ l \in \mathcal{L}, \tag{1}$$

where $\mathcal{L} \triangleq [1, \ldots, L]$, $\mathbf{S} \in \mathbb{C}^{N_t \times L}$ is the transmit signal matrix from the BS over the L time slots, $\mathbf{S}(:,l)$ denotes the lth column of $\mathbf{S}$, and $n_{u_k}[l] \sim \mathcal{CN}(0, \sigma^2)$ is the noise received at the kth user. Besides, the channels are modeled as $\mathbf{G} \triangleq \sqrt{l_{br}}\bar{\mathbf{G}} \in \mathbb{C}^{N \times N_t}$ and $\mathbf{h}_{u_k}^H \triangleq \sqrt{l_{ru_k}}\bar{\mathbf{h}}_{u_k}^H \in \mathbb{C}^{1 \times N}$, where l_{xy} is the large-scale path loss of the link x-to-y and $xy \in \{br, ru_k\}$ denotes the direction of the link from x to y. Furthermore, the small-scale fading coefficients $\bar{\mathbf{G}} \in \mathbb{C}^{N \times N_t}$ and $\bar{\mathbf{h}}_{u_k}^H \in \mathbb{C}^{1 \times N_t}$ are modeled as Rician fading channels [29], [48], given by

$$\bar{\mathbf{G}} = \sqrt{\frac{\kappa_{\text{G}}}{1+\kappa_{\text{G}}}}\bar{\mathbf{G}}_{\text{LOS}} + \sqrt{\frac{1}{1+\kappa_G}}\bar{\mathbf{G}}_{\text{NLOS}}, \tag{2}$$

$$\bar{\mathbf{h}}_{u_k}^H = \sqrt{\frac{\kappa_{u_k}}{1+\kappa_{u_k}}}\bar{\mathbf{h}}_{u_k,\text{LOS}} + \sqrt{\frac{1}{1+\kappa_{u_k}}}\bar{\mathbf{h}}_{u_k,\text{NLOS}}^H, \tag{3}$$

respectively, where $\kappa_{\text{G}} \geq 0$ and $\kappa_{u_k} \geq 0$ are the corresponding Rician factors. $\bar{\mathbf{G}}_{\text{NLOS}}$ and $\bar{\mathbf{h}}_{u_k,\text{NLOS}}^H$ are the non-line-of-sight (NLOS) components which are modeled as Rayleigh fading channels. Denoting ω_B and ω_R as the effective angle-of-departure (AOD) and angle-of-arrival (AOA) of the link BS-to-STAR-RIS, respectively, the line-of-sight (LOS) channel from the BS to the STAR-RIS is $\bar{\mathbf{G}}_{\text{LOS}} \triangleq \mathbf{a}_N^T(\omega_R)\,\mathbf{a}_{N_t}(\omega_B)$, where the steering vectors are respectively given by[3]

$$\mathbf{a}_N(\omega_R) = \frac{1}{\sqrt{N}}\left[1, e^{-j2\pi\frac{\sin(\omega_R)}{2}}, \ldots, e^{-j2\pi\frac{(N-1)\sin(\omega_R)}{2}}\right]^T, \tag{4}$$

$$\mathbf{a}_{N_t}(\omega_B) = \frac{1}{\sqrt{N_t}}\left[1, e^{-j2\pi\frac{\sin(\omega_B)}{2}}, \ldots, e^{-j2\pi\frac{(N_t-1)\sin(\omega_B)}{2}}\right]^T. \tag{5}$$

Accordingly, the LOS channel from the STAR-RIS to the kth user is modeled as $\bar{\mathbf{h}}_{u_k,\text{LOS}} \triangleq \mathbf{a}_N(\omega_{u_k})$, where $\mathbf{a}_N(\omega_{u_k})$ is the steering vector with the effective AOD, ω_{u_k}.

In the following, we first outline the CI principle, where the multiuser interference can be harnessed and become beneficial if it can push the received signals farther away from the decision boundaries by getting them deeper into the detection region for improving the signal detection performance. Taking the quadrature-PSK (QPSK) modulation as an example, the CI principle is illustrated in Fig. 2, where $\Phi = \pi/4$ and the green sectors are the decision regions that benefit the signal demodulation at the intended user. Specifically, vector $\overrightarrow{\text{OD}}$ denotes the interference-free signal and $\Gamma_{u_k} = \frac{\left|\overrightarrow{\text{OD}}\right|^2}{\sigma^2}$. Besides, vector $\overrightarrow{\text{OC}} = \mathbf{h}_k^H\mathbf{S}(:,l)$ is the signal received at the kth user during the lth time slot. Clearly, the signal is located at the CI region if and only if $\left|\left|\overrightarrow{\text{AB}}\right|\right| - \left|\left|\overrightarrow{\text{AC}}\right|\right| \geq 0$ [18]. The analytical result of the difference $\left|\left|\overrightarrow{\text{AB}}\right|\right| - \left|\left|\overrightarrow{\text{AC}}\right|\right|$ can be derived from Fig. 2 and the condition for advocating the CI region is given by [18]

$$\mathcal{R}\left(\mathbf{h}_{u_k}^H\mathbf{\Theta}_t\mathbf{G}\mathbf{S}(:,l) - \sigma\sqrt{\Gamma_{u_k}}\right)\sin(\Phi) - \left|\mathcal{I}\left(\mathbf{h}_{u_k}^H\mathbf{\Theta}_t\mathbf{G}\mathbf{S}(:,l)\right)\right|\cos(\Phi) \geq 0. \tag{6}$$

Since $\mathbf{S}(:,l) = \mathbf{S}\mathbf{e}_l$, where $\mathbf{e}_l$ is the lth column of an $L \times L$ identity matrix, by employing [50, eq. (1.11.18)], a compact

[3]Similar to [49], the reflector of STAR-RIS is assumed to be a uniform linear array for simplicity and the proposed algorithm can be directly generalized to the case of adopting a planar array model.

form of constraint (6) can be derived as

$$\mathcal{R}\left(\tilde{\mathbf{h}}_{l,k}^{H}\left(\boldsymbol{\Theta}_t\right)\mathbf{s}\right)\geq\gamma_{u_k},\ \mathcal{I}\left(\hat{\mathbf{h}}_{l,k}^{H}\left(\boldsymbol{\Theta}_t\right)\mathbf{s}\right)\geq\gamma_{u_k}, \tag{7}$$

where $\mathbf{s}=\mathrm{vec}\left(\mathbf{S}\right)$, $\gamma_{u_k}\triangleq\sigma\sqrt{\Gamma_{u_i}}\sin\Phi$. $\tilde{\mathbf{h}}_{l,k}^{H}\left(\boldsymbol{\Theta}_t\right)$ and $\hat{\mathbf{h}}_{l,k}^{H}\left(\boldsymbol{\Theta}_t\right)$ are given by

$$\tilde{\mathbf{h}}_{l,k}^{H}\left(\boldsymbol{\Theta}_t\right)\triangleq\mathbf{e}_{l,L}^{T}\otimes\left(\mathbf{h}_{u_k}^{H}\boldsymbol{\Theta}_t\mathbf{G}\right)e^{-j\angle x_k(l)}\left(\sin(\Phi)+e^{-j\frac{\pi}{2}}\cos(\Phi)\right), \tag{8}$$

$$\hat{\mathbf{h}}_{l,k}^{H}\left(\boldsymbol{\Theta}_t\right)\triangleq\mathbf{e}_{l,L}^{T}\otimes\left(\mathbf{h}_{u_k}^{H}\boldsymbol{\Theta}_t\mathbf{G}\right)e^{-j\angle x_k(l)}\left(\sin(\Phi)-e^{-j\frac{\pi}{2}}\cos(\Phi)\right), \tag{9}$$

where $\angle x_k(l)$ is the angle of symbol $x_k(l)$. Note that the extension to other practical modulation schemes can be realized directly by expressing the corresponding constructive region using different linear inequalities of $\mathcal{R}\left(\tilde{\mathbf{h}}_{l,k}^{H}\left(\boldsymbol{\Theta}_t\right)\mathbf{s}\right)$ and $\mathcal{I}\left(\hat{\mathbf{h}}_{l,k}^{H}\left(\boldsymbol{\Theta}_t\right)\mathbf{s}\right)$. Particularly, the proposed joint optimization algorithm can be adapted to other modulation schemes directly if the signal decision region is convex [11], [51], [52].

C. Radar Sensing Performance Metric

The signals from the BS and the STAR-RIS are superimposed at the kth radar targets in the lth time slot, which is given by

$$y_{r_k}(l)=\left(\sqrt{l_{bu_k}}\mathbf{a}_{N_t}^{T}(\psi_k)+\sqrt{l_{ru_k}}\mathbf{a}_{N}^{T}(\theta_k)\boldsymbol{\Theta}_r\mathbf{G}\right)\mathbf{S}(:,l),\quad\forall k\in\mathcal{K}_e, \tag{10}$$

where l_{bu_k} is the path loss from the BS to the kth target and l_{ru_k} is the path loss from STAR-RIS to the kth target. Besides, $\mathcal{K}_e\triangleq\{1\ldots,K_e\}$, ψ_k and θ_k are the effective AOD from the BS and the STAR-RIS to the kth radar target. Furthermore, $\mathbf{a}_{N_t}(\psi_k)$ is the steering vector from the BS to the kth target and $\mathbf{a}_N(\theta_k)$ is the steering vector from the STAR-RIS to the kth target [45]. Accordingly, the average beampattern over the L time slots at the kth target direction can be derived as [47]

$$P(\theta_k,\psi_k)=\frac{\mathbf{b}\left(\psi_k,\theta_k\right)\mathbf{S}\mathbf{S}^{H}\mathbf{b}^{H}\left(\psi_k,\theta_k\right)}{L},\ k\in\mathcal{K}_e, \tag{11}$$

where $\mathbf{b}\left(\psi_k,\theta_k\right)=\sqrt{l_{bu_k}}\mathbf{a}_{N_t}^{T}(\psi_k)+\sqrt{l_{ru_k}}\mathbf{a}_{N}^{T}(\theta_k)\boldsymbol{\Theta}_r\mathbf{G}$, and the angles ψ_k and θ_k are determined by the relative locations of the kth target, the STAR-RIS, and the BS [24], [53]. Besides, having a low peak-to-average-power ratio (PAPR) is an important characteristic of modern radar systems [47] and the corresponding constraint is expressed as

$$\max_{1\leq l\leq L}|\mathbf{S}(:,l)|^2/\left(\frac{1}{N_tL}\mathbf{s}^{H}\mathbf{s}\right)\leq\eta. \tag{12}$$

D. Secure Communication Performance Metric

As pointed out by [37], [38], different from the traditional radar probing signals, the DFRC probing signals also carry information and increasing the radiation power towards to multiple malicious radar targets increases the potential of information leakage, which may bring security challenges. Hence, the probing signals should be designed carefully to maximize the received illumination power at the multiple target directions while securing the confidential information contained in the probing signals. To deceive the malicious targets, some works have proposed to manipulate the confidential signal wiretapped at the targets by forcing the signal to fall into the destructive region for detection [38], [54], denoted as red-shaded region in Fig. 2. In such a case, the signals received at the sensing targets are pushed away from the correct decision region such that accuracy detection at those Eves becomes challenging or even impossible [54]. Although the above method can guarantee communication security to a certain extent, [55] shows the potential security threat encountered by the above transmission scheme in the presence of smart Eves. In particular, the smart Eves may infer the secure transmission scheme adopted by the transmitter from the historical observations and confirm that the received signal deviates from the constructive region. Accordingly, it can tactfully recalibrate the decision boundary in signal detection according to the position relation between the destructive region and the constellation point. Taking the binary phase shift keying (BPSK) constellation as an example, when the lth transmitted symbol $x[l]=1$, the designed signal mistakes the wiretapped symbol at the Eve lie in the destructive region, such that Eve estimates $x[l]$ as -1 by mistake [55]. However, Eve can still infer the correct symbol estimate $x[l]=1$ by exploiting the side information inherent in the known incorrect decision.

To handle the security threat above, inspired by [55], we propose to utilize the unclassified signal broadcasted to public users for deceiving multiple malicious radar targets concurrently. In particular, with the symbol-level precoding technique, the unclassified signal is designed to lie in the constructive region of multiple radar targets. Then, malicious targets mistake the unclassified signal for confidential signals, which protects the confidential information from wiretapping. To guarantee an effective deception, the minimum Euclidean distance from the noise-free wiretapped signal to the decision boundary of any public signals is adopted as the QoS, given by

$$\mathcal{R}\left(\tilde{\mathbf{g}}_{l,k}^{H}\left(\boldsymbol{\Theta}_r\right)\mathbf{s}\right)\geq\eta_{e_k},\ \mathcal{I}\left(\hat{\mathbf{g}}_{l,k}^{H}\left(\boldsymbol{\Theta}_r\right)\mathbf{s}\right)\geq\eta_{e_k},\forall k\in\mathcal{K}_e, \tag{13}$$

where $\eta_{e_k}\triangleq\sigma\sqrt{\Gamma_{e_k}}\sin(\Phi)$, $\tilde{\mathbf{g}}_{l,k}^{H}$ and $\hat{\mathbf{g}}_{l,k}^{H}$ are given by

$$\tilde{\mathbf{g}}_{l,k}^{H}\left(\boldsymbol{\Theta}_r\right)\triangleq\mathbf{e}_{l,L}^{T}\otimes\left(\mathbf{t}_{e_k}^{H}+\mathbf{g}_{e_k}^{H}\boldsymbol{\Theta}_r\mathbf{G}\right)\times e^{-j\angle x_{\hat{u}}(l)}\left(\sin(\Phi)+e^{-j\frac{\pi}{2}}\cos(\Phi)\right), \tag{14}$$

$$\hat{\mathbf{g}}_{l,k}^{H}\left(\boldsymbol{\Theta}_r\right)\triangleq\mathbf{e}_{l,L}^{T}\otimes\left(\mathbf{t}_{e_k}^{H}+\mathbf{g}_{e_k}^{H}\boldsymbol{\Theta}_r\mathbf{G}\right)e^{-j\angle x_{\hat{u}}(l)}\times\left(\sin(\Phi)-e^{-j\frac{\pi}{2}}\cos(\Phi)\right), \tag{15}$$

respectively, where $x_{\hat{u}}(l)$ denotes the symbol intended to any public user in the lth slot. Besides, we have

$$\mathbf{g}_{l,k}^{H}=\sqrt{\frac{\kappa_{\mathbf{g}_{l,k}}}{1+\kappa_{\mathbf{g}_{l,k}}}}\mathbf{a}_{N}^{T}(\theta_k)+\sqrt{\frac{1}{1+\kappa_{\mathbf{g}_{l,k}}}}\mathbf{g}_{l,k,\mathrm{NLOS}}^{H}, \tag{16}$$

$$\mathbf{t}_{l,k}^{H}=\sqrt{\frac{\kappa_{\mathbf{t}_{l,k}}}{1+\kappa_{\mathbf{t}_{l,k}}}}\mathbf{a}_{N_t}^{T}(\psi_k)+\sqrt{\frac{1}{1+\kappa_{\mathbf{t}_{l,k}}}}\mathbf{t}_{l,k,\mathrm{NLOS}}^{H}. \tag{17}$$

The components in (16) and (17) are defined similarly as their counterparts in (2) and (3), respectively. Constraint (13) restricts the wiretapped signal received at the multiple radar targets to fall into the decision region that favours any public

signals to deceive the malicious targets. Besides, different from the block-level secure precoding which can only provide statistical security guarantees [12], [44], our adopted performance metric can ensure them at the symbol-level.

E. Joint Optimization Problem Formulation

Based on the performance metrics above, the joint design of the waveform, transmit and reflective beamforming $(\mathbf{\Theta}_t, \mathbf{\Theta}_r)$ can be formulated as the following problem

$$\underset{\mathbf{s},\mathbf{\Theta}_t,\mathbf{\Theta}_r}{\text{maximize}} \sum_{i=1}^{K_e} P(\theta_i,\psi_i) \tag{18a}$$

$$\text{s.t. } ||\mathbf{s}-\mathbf{s}_0||_2 \le \sqrt{\epsilon L}, \tag{18b}$$

$$\mathbf{s}^H\mathbf{s} = LP_t, \tag{18c}$$

$$\mathbf{s}^H\mathbf{E}_m\mathbf{s} \le \frac{P_t\eta}{N_t},\ 1\le m\le N_tL, \tag{18d}$$

$$(7),\ (13),\ k\in\mathcal{K}_u,\ k\in\mathcal{K}_e,\ l\in\mathcal{L}, \tag{18e}$$

$$[\mathbf{\Theta}_r]_{m,m}^2 + [\mathbf{\Theta}_t]_{m,m}^2 = 1,\ 1\le m\le N, \tag{18f}$$

where ϵ is a customized parameter for controlling the similarity level, and constraint (18b) is the l_2 norm similarity constraint for shaping the transmission signal waveform to mimic the reference signal $\mathbf{s}_0$, e.g., pulse compression [47]. Constraints (18c) and (18d) denote the PAPR constraint (12) [47]. Besides, $\mathbf{E}_m$ is an $N_tL\times N_tL$ diagonal matrix whose (m,m) element is either 1 or 0. Constraint (18f) denotes the amplitude constraints on the transmission and reflection elements [30]. Similar to [45], [56], [57], the objective of the joint optimization is to maximize the average total illumination power at the target directions, i.e., $\sum_{i=1}^{K_e} P(\theta_i,\psi_i)$.

It is clear that problem (18) is nonconvex. Although its globally optimal solution can be derived by exploiting global optimization methods, which have exponential complexity and thus are not suitable for practical design [58]. Specifically, the couplings among $\mathbf{s}$, $\mathbf{\Theta}_t$, and $\mathbf{\Theta}_r$ complicates the overall solution development. Besides, constraints (18c) and (18d) are both nonconvex. Even worse, for fixed $\mathbf{\Theta}_t$ and $\mathbf{\Theta}_r$, the objective function is nonconvex with respect to $\mathbf{s}$, and the same holds for $\mathbf{\Theta}_t$ and $\mathbf{\Theta}_r$. Besides, except for the nonconvexity, there is a large number of quadratic and linear constraints in (18d) and (18e), which renders the computational complexity of handling problem (18) exceedingly high. Therefore, it is desirable to design an efficient algorithm to handle this nonconvex problem. In the next section, we propose a low-complexity distance-majorization induced iterative algorithm.

Remark 1: Different from the traditional RIS technology, STAR-RIS divides a service area into a reflection space and a transmission space [32]. Therefore, a user can only be served by $\mathbf{\Theta}_r$ or $\mathbf{\Theta}_t$, depending on its location. To simplify the presentation, this work follows [36] to design $\mathbf{\Theta}_r$ and $\mathbf{\Theta}_t$ for achieving sensing and communications, respectively. Our proposed joint optimization algorithm can be generalized to the scenario where communication users and sensing targets coexist in some common spaces. In particular, $\mathbf{\Theta}_r$ and $\mathbf{\Theta}_t$ should be designed to achieve radar sensing and information transmission simultaneously. Such a generalization is straightforward which can be achieved by including $\mathbf{\Theta}_r$ into the beampattern and introducing communication QoS constraints as functions of $\mathbf{\Theta}_t$.

III. Distance-Majorization Induced Low-Complexity Algorithm

To handle the coupling among $\mathbf{s}$, $\mathbf{\Theta}_t$, and $\mathbf{\Theta}_r$, we first employ the alternating optimization (AO) algorithm to decompose problem (18) into two subproblems: optimizing $\mathbf{S}$ and $(\mathbf{\Theta}_t, \mathbf{\Theta}_r)$ alternately. Then, a customized distance-majorization based algorithm is developed for handling the subproblem in each iteration.

A. Distance-Majorization Algorithm for Optimizing the Signal Waveform

With fixed $\mathbf{\Theta}_t$ and $\mathbf{\Theta}_r$, by employing [50, eq. (1.11.18)], the optimization of the transmission waveform $\mathbf{s}$ can be formulated as follows

$$\underset{\mathbf{s}}{\text{maximize}}\ \mathbf{s}^H\mathbf{B}\mathbf{s} \tag{19a}$$

$$\text{s.t. } ||\mathbf{s}||_2^2 = LP_t,\ |\mathbf{S}(i,l)|^2 \le \frac{P_t\eta}{N_t},\ 1\le i\le N_t,\ 1\le l\le L, \tag{19b}$$

$$\mathcal{R}\left(-\tilde{\mathbf{h}}_{l,k}^H(\mathbf{\Theta}_t)\,\mathbf{s}\right) \le -\gamma_{u_k},\ \mathcal{R}\left(-\hat{\mathbf{h}}_{l,k}^H(\mathbf{\Theta}_t)\,\mathbf{s}\right) \le -\gamma_{u_k},\ k\in\mathcal{K}_u,\ l\in\mathcal{L}, \tag{19c}$$

$$\mathcal{R}\left(-\tilde{\mathbf{g}}_{l,k}^H(\mathbf{\Theta}_r)\,\mathbf{s}\right) \le -\eta_{e_k},\ \mathcal{R}\left(-\hat{\mathbf{g}}_{l,k}^H(\mathbf{\Theta}_r)\,\mathbf{s}\right) \le -\eta_{e_k},\ k\in\mathcal{K}_e,\ l\in\mathcal{L}, \tag{19d}$$

$$||\mathbf{s}-\mathbf{s}_0||_2 \le \sqrt{\epsilon L}, \tag{19e}$$

where $\mathbf{A}(\psi_i,\theta_i) \triangleq \mathbf{b}^H(\psi_i,\theta_i)\,\mathbf{b}(\psi_i,\theta_i)$ and $\mathbf{B} = \sum_{i=1}^{K_e}(\mathbf{I}_L\otimes\mathbf{A}(\psi_i,\theta_i))$.

Following [11], [24], the obstacle introduced by the objective function (19a) and the constant transmit power constraint in (19b) can be addressed by applying the ADMM and majorization-minimization (MM) jointly. The details are given in Appendix A. However, since there are N_tL quadratic constraints and $2(K_u+K_e)L$ linear inequality constraints in the subproblem, the overall computational complexity for solving problem (60) in Appendix A is at least $\mathcal{O}(1)\,(2(K_u+K_e)L+N_tL+1)^{\frac{1}{2}}\,N_tL\left((N_tL)^2+2(K_u+K_e)L+2N_tL\right)$ [59], which is exceedingly high. In particular, as pointed out in [11, Section IV], although the ADMM-induced algorithm is efficient for small-scale cases, its computational complexity becomes prohibitive, especially when L, K_u, and K_e become large.

To design an efficient algorithm to handle problem (19), we propose a distance-majorization induced iterative algorithm. In particular, we employ the Courant's penalty method [60] to incorporate constraints (19b)-(19d) into the objective function, and then, a distance-majorization induced low-complexity algorithm is proposed to handle the problem with the modified objective function [61], [62]. To facilitate the algorithm design, we first convert the complex-valued formulation of problem

(19) into its real-valued counterpart by exploiting the following identity

$$\begin{bmatrix}\mathcal{R}\left(\mathbf{Bs}\right)\\ \mathcal{I}\left(\mathbf{Bs}\right)\end{bmatrix}=\begin{bmatrix}\mathcal{R}(\mathbf{B}), & -\mathcal{I}(\mathbf{B})\\ \mathcal{I}(\mathbf{B}), & \mathcal{R}(\mathbf{B})\end{bmatrix}\begin{bmatrix}\mathcal{R}(\mathbf{s})\\ \mathcal{I}(\mathbf{s})\end{bmatrix}. \tag{20}$$

In particular, the real and imaginary parts of $-\tilde{\mathbf{h}}_{u_k}^H\left(\mathbf{\Theta}_t\right)\mathbf{s}$ can be written in a compact matrix form which is given by

$$\begin{bmatrix}\mathcal{R}\left(-\tilde{\mathbf{h}}_{l,k}^H\left(\mathbf{\Theta}_t\right)\mathbf{s}\right)\\ \mathcal{I}\left(-\tilde{\mathbf{h}}_{l,k}^H\left(\mathbf{\Theta}_t\right)\mathbf{s}\right)\end{bmatrix}\triangleq-\begin{bmatrix}\mathcal{R}\left(\tilde{\mathbf{h}}_{l,k}^H\left(\mathbf{\Theta}_t\right)\right), & -\mathcal{I}\left(\tilde{\mathbf{h}}_{l,k}^H\left(\mathbf{\Theta}_t\right)\right)\\ \mathcal{I}(\tilde{\mathbf{h}}_{l,k}^H\left(\mathbf{\Theta}_t\right)), & \mathcal{R}\left(\tilde{\mathbf{h}}_{l,k}^H\left(\mathbf{\Theta}_t\right)\right)\end{bmatrix}\times\begin{bmatrix}\mathcal{R}\left(\mathbf{s}\right)\\ \mathcal{I}\left(\mathbf{s}\right)\end{bmatrix}.$$

Defining $\tilde{\mathbf{f}}_{l,k}^H\left(\mathbf{\Theta}_t\right)\triangleq-\left[\mathcal{R}\left(\tilde{\mathbf{h}}_{l,k}^H\left(\mathbf{\Theta}_t\right)\right),-\mathcal{I}\left(\tilde{\mathbf{h}}_{l,k}^H\left(\mathbf{\Theta}_t\right)\right)\right]$, the first constraint in (19c) can be reformulated as $\tilde{\mathbf{f}}_{u_k}^H\hat{\mathbf{s}}\leq-\gamma_{u,k}$. Accordingly, the real-valued version of problem (19) can be formulated as

$$\begin{aligned}&\underset{\mathbf{s}}{\text{maximize}}\ \hat{\mathbf{s}}^T\hat{\mathbf{B}}\hat{\mathbf{s}}\\ &\text{s.t. }||\hat{\mathbf{s}}||_2^2=LP_t,\ ||\left[\hat{\mathbf{s}}(n),\hat{\mathbf{s}}(LN_t+n)\right]||_2^2\leq\frac{P_t\eta}{N_t},\qquad(21a)\\ &\quad\tilde{\mathbf{f}}_{l,k}^T\left(\mathbf{\Theta}_t\right)\hat{\mathbf{s}}\leq-\gamma_{u_k},\ \hat{\mathbf{f}}_{l,k}^T\left(\mathbf{\Theta}_t\right)\hat{\mathbf{s}}\leq-\gamma_{u_k},k\in\mathcal{K}_u,\ l\in\mathcal{L},\qquad(21b)\\ &\quad\tilde{\mathbf{t}}_{l,j}^T\left(\mathbf{\Theta}_r\right)\hat{\mathbf{s}}\leq-\eta_{e_j},\ \hat{\mathbf{t}}_{l,j}^T\left(\mathbf{\Theta}_r\right)\hat{\mathbf{s}}\leq-\eta_{e_j},j\in\mathcal{K}_e,\ l\in\mathcal{L},\qquad(21c)\\ &\quad||\hat{\mathbf{s}}-\hat{\mathbf{s}}_0||_2\leq\sqrt{\epsilon L},\qquad(21d)\end{aligned}$$

where $\hat{\mathbf{s}}=\left[\mathcal{R}(\mathbf{s}),\mathcal{I}\left(\mathbf{s}\right)\right]^T$, $\hat{\mathbf{s}}_0=\left[\mathcal{R}(\mathbf{s}_0),\mathcal{I}\left(\mathbf{s}_0\right)\right]^T$,

$$\hat{\mathbf{B}}=\begin{bmatrix}\mathcal{R}\left(\mathbf{B}\right), & -\mathcal{I}\left(\mathbf{B}\right)\\ \mathcal{I}\left(\mathbf{B}\right), & \mathcal{R}\left(\mathbf{B}\right)\end{bmatrix}, \tag{22}$$

$$\hat{\mathbf{f}}_{l,k}^T\left(\mathbf{\Theta}_t\right)=-\left[\mathcal{R}\left(\hat{\mathbf{h}}_{l,k}^T\right),-\mathcal{I}\left(\hat{\mathbf{h}}_{l,k}^T\right)\right], \tag{23}$$

$$\tilde{\mathbf{t}}_{l,k}^T\left(\mathbf{\Theta}_t\right)=-\left[\mathcal{R}\left(\tilde{\mathbf{g}}_{l,k}^T\right),-\mathcal{I}\left(\tilde{\mathbf{g}}_{l,k}^T\right)\right], \tag{24}$$

$$\hat{\mathbf{t}}_{l,k}^T\left(\mathbf{\Theta}_t\right)=-\left[\mathcal{R}\left(\hat{\mathbf{g}}_{l,k}^T\right),-\mathcal{I}\left(\hat{\mathbf{g}}_{l,k}^T\right)\right]. \tag{25}$$

To handle the nonconvex optimization problem (21), we first apply the Courant's penalty method [60] to incorporate constraints (21a), (21b), and (21c) into the objective function and reformulate the nonconvex maximization as follows:

$$\begin{aligned}&\underset{\hat{\mathbf{s}},\tilde{y}_k^u,\hat{y}_k^u,\tilde{y}_k^e,\hat{y}_k^e}{\text{maximize}}\ \hat{\mathbf{s}}^T\hat{\mathbf{B}}\hat{\mathbf{s}}-\frac{\rho}{2}\Delta\left(\hat{\mathbf{s}}\right)\qquad(26a)\\ &\text{s.t. }\tilde{y}_{l,k}^u=\tilde{\mathbf{f}}_{l,k}^H\left(\mathbf{\Theta}_t\right)\hat{\mathbf{s}},\ \hat{y}_{l,k}^u=\hat{\mathbf{f}}_{l,k}^H\left(\mathbf{\Theta}_t\right)\hat{\mathbf{s}},\ k\in\mathcal{K}_u,\ l\in\mathcal{L},\\ &\quad\tilde{y}_{l,j}^e=\tilde{\mathbf{t}}_{l,k}^H\left(\mathbf{\Theta}_r\right)\hat{\mathbf{s}},\ \hat{y}_{l,j}^e=\hat{\mathbf{t}}_{l,k}^H\left(\mathbf{\Theta}_r\right)\hat{\mathbf{s}},\ j\in\mathcal{K}_e,\ l\in\mathcal{L},\\ &\quad||\hat{\mathbf{s}}-\hat{\mathbf{s}}_0||_2\leq\sqrt{\epsilon L},\qquad(26b)\end{aligned}$$

where $\rho>0$ is the penalty parameter and

$$\begin{aligned}\Delta\left(\hat{\mathbf{s}}\right)\triangleq&\sum_{k=1}^{K_u}\sum_{l=1}^{L}\left(\text{dist}^2\left(\tilde{y}_{l,k}^u,\Xi\right)+\text{dist}^2\left(\hat{y}_{l,k}^u,\Xi\right)\right)+\text{dist}^2\left(\hat{\mathbf{s}},\Omega\right)\\&+\sum_{j=1}^{K_e}\sum_{l=1}^{L}\left(\text{dist}^2\left(\hat{y}_{l,j}^e,\Psi\right)+\text{dist}^2\left(\tilde{y}_{l,j}^e,\Psi\right)\right).\end{aligned}$$

Besides, Ω, Ξ, and Ψ are feasible sets determined by constraints (21a), (21b), and (21c), respectively.

Theorem 1: As $\rho\to+\infty$, the solution obtained by solving problem (26) converges to the optimal solution of problem (21).

Proof: The proof is given in Appendix B. ■

Although constraints (21a), (21b), and (21c) have been incorporated into the objective function, calculating the minimum distance $\Delta\left(\hat{\mathbf{s}}\right)$ still involves solving multiple optimization problems whose computational complexity can be exceedingly high. As an alternative, by employing MM [63], we convert problem (26) into a sequence of convex optimization problems whose solutions can be calculated in closed-form. In the following, we take $\text{dist}^2\left(\tilde{y}_{l,i}^u,\Xi\right)$ as an example to show the details.

Firstly, since the function $\text{dist}^2\left(\tilde{y}_{l,i}^u,\Xi\right)$ is convex in $\tilde{y}_{l,i}^u$ [64, Section 3.2.5], the first-order Taylor expansion establishes a surrogate function of $\text{dist}^2\left(\tilde{y}_{l,i}^u,\Xi\right)$. Therefore, the key step is to obtain the gradient of $\text{dist}^2\left(\tilde{y}_{l,i}^u,\Xi\right)$ with respect to $\tilde{y}_{l,i}^u$. Before proceeding, we first introduce Hadamard semidifferentials [63], defined as follows.

Definition 1: A function $f(\mathbf{x})$ is Hadamard semidifferentiable at $\mathbf{x}$ if the following limit holds for any vector $\mathbf{v}$

$$\lim_{w\to v,t\to0}\frac{f\left(\mathbf{x}+t\mathbf{w}\right)-f\left(\mathbf{x}\right)}{t}=d_vf(\mathbf{x}). \tag{27}$$

Besides, from [63, Proposition 3.2.1], we have $d_vf(\mathbf{x})=df(\mathbf{x})\mathbf{v}$, where $df(\mathbf{x})$ is the Jacobi matrix. Moreover, as shown in [63, Example 3.2.14], we have

$$d_v\text{dist}\left(\tilde{y}_{l,k}^u,\Xi\right)=\inf_{w\in\Xi}\frac{\left(\tilde{y}_{l,k}^u-w\right)v}{||\tilde{y}_{l,k}^u-w||}=\inf_{w\in\Xi}\frac{\left(\tilde{y}_{l,k}^u-w\right)v}{\text{dist}\left(\tilde{y}_{l,k}^u,\Xi\right)}.$$

Since Ξ is convex, $\inf_{w\in\Xi}$ reduces to the projected point $\tilde{\gamma}_{u,k}$ that is obtained by projecting $\tilde{\mathbf{f}}_{l,k}^H\left(\mathbf{\Theta}_t\right)\hat{\mathbf{s}}$ onto the set defined by (21b). Accordingly, the gradient of $\text{dist}\left(\tilde{y}_{l,k}^u,\Xi\right)$ with respect to $\tilde{y}_{l,k}^u$ can be derived as

$$\nabla_{\tilde{y}_{l,k}^u}\text{dist}\left(\tilde{y}_{l,k}^u,\Xi\right)=\frac{\tilde{y}_{l,k}^u-\tilde{\gamma}_{u_k}}{\text{dist}\left(\tilde{y}_{l,k}^u,\Xi\right)}. \tag{28}$$

Then, without considering the constant terms, a surrogate function of the objective function in (26a) is represented as

$$\begin{aligned}F\left(\hat{\mathbf{s}}\right)\triangleq&\ \hat{\mathbf{s}}^T\hat{\mathbf{B}}\hat{\mathbf{s}}-\frac{\rho}{2}\sum_{k=1}^{K_u}\sum_{l=1}^{L}\left|\left|\tilde{y}_{l,k}^u-\tilde{\gamma}_{u_k}\right|\right|_2^2\\&-\frac{\rho}{2}\left(\sum_{k=1}^{K_u}\sum_{l=1}^{L}\left|\left|\hat{y}_{l,k}^u-\hat{\gamma}_{u_k}\right|\right|_2^2+\sum_{j=1}^{K_e}\sum_{l=1}^{L}\left|\left|\hat{y}_{l,j}^e-\hat{\eta}_{e_j}\right|\right|_2^2\right)\\&-\frac{\rho}{2}\sum_{j=1}^{K_e}\sum_{l=1}^{L}\left|\left|\tilde{y}_{l,j}^e-\tilde{\eta}_{e_j}\right|\right|_2^2-\frac{\rho}{2}\left|\left|\hat{\mathbf{s}}-\check{\mathbf{s}}\right|\right|_2^2-\frac{\rho}{2}\left|\left|\hat{\mathbf{s}}-\bar{\mathbf{s}}\right|\right|_2^2,\end{aligned}$$

where $\check{\mathbf{s}}$ and $\bar{\mathbf{s}}$ are the solutions obtained by projecting $\mathbf{s}$ onto the sets $\check{\Omega}\triangleq\left\{\mathbf{s}|\ ||\hat{\mathbf{s}}||_2^2=LP_t\right\}$ and $\bar{\Omega}\triangleq\left\{\mathbf{s}|\ ||\left[\hat{\mathbf{s}}(n),\hat{\mathbf{s}}(LN_t+n)\right]||_2^2\leq\frac{P_t\eta}{N_t}\right\}$, respectively. Moreover, $\hat{\gamma}_{u_k}$, $\tilde{\gamma}_{u_k}$, $\hat{\eta}_{e_k}$, and $\tilde{\eta}_{e_k}$ are the ones obtained by projecting $\tilde{\mathbf{f}}_{l,k}^H\left(\mathbf{\Theta}_t\right)\hat{\mathbf{s}}$, $\hat{\mathbf{f}}_{l,k}^H\left(\mathbf{\Theta}_t\right)\hat{\mathbf{s}}$, $\tilde{\mathbf{t}}_{l,j}^H\left(\mathbf{\Theta}_t\right)\hat{\mathbf{s}}$, and $\hat{\mathbf{t}}_{l,j}^H\left(\mathbf{\Theta}_t\right)\hat{\mathbf{s}}$ onto the

feasible sets defined by (21b) and (21c), respectively.

Finally, problem (26) can be approximated as

$$\underset{\hat{\mathbf{s}}}{\text{maximize}}\ F\left(\hat{\mathbf{s}}\right),\ \text{s.t. (26}b\text{)}. \tag{29}$$

Although problem (29) is still nonconvex due to the nonconvexity of $F\left(\hat{\mathbf{s}}\right)$, its optimal solution still satisfies the KKT condition [64, Section 5.2], given by

$$\begin{aligned}&-2\hat{\mathbf{B}}\hat{\mathbf{s}}+\rho\left(\hat{\mathbf{s}}-\breve{\mathbf{s}}\right)+\rho\left(\hat{\mathbf{s}}-\tilde{\mathbf{s}}\right)+2\lambda\left(\hat{\mathbf{s}}-\hat{\mathbf{s}}_0\right)\\&+\sum_{l,k}\left(\tilde{\lambda}_{l,k}^{u,s}\tilde{\mathbf{f}}_{l,k}\left(\boldsymbol{\Theta}_t\right)+\hat{\lambda}_{l,k}^{u,s}\hat{\mathbf{f}}_{l,k}\left(\boldsymbol{\Theta}_t\right)\right)\\&+\sum_{l,j}\left(\tilde{\lambda}_{l,j}^{e,s}\tilde{\mathbf{t}}_{l,j}\left(\boldsymbol{\Theta}_t\right)+\hat{\lambda}_{l,j}^{e,s}\hat{\mathbf{t}}_{l,j}\left(\boldsymbol{\Theta}_t\right)\right)=0,\end{aligned} \tag{30}$$

$$\lambda\left(\left|\left|\hat{\mathbf{s}}-\hat{\mathbf{s}}_0\right|\right|_2-\sqrt{\epsilon L}\right)=0, \tag{31}$$

$$\rho\left(\tilde{y}_{l,k}^{u}-\tilde{r}_{u_k}\right)-\tilde{\lambda}_{l,k}^{u,s}=0, \tag{32}$$

$$\rho\left(\hat{y}_{l,k}^{u}-\hat{r}_{u_k}\right)-\hat{\lambda}_{l,k}^{u,s}=0, \tag{33}$$

$$\rho\left(\tilde{y}_{l,j}^{e}-\tilde{\eta}_{e_j}\right)-\tilde{\lambda}_{l,j}^{e,s}=0, \tag{34}$$

$$\rho\left(\hat{y}_{l,j}^{e}-\hat{\eta}_{e_j}\right)-\hat{\lambda}_{l,j}^{e,s}=0, \tag{35}$$

where λ, $\tilde{\lambda}_{l,k}^{u,s}$, $\hat{\lambda}_{l,k}^{u,s}$, $\tilde{\lambda}_{l,j}^{e,s}$, and $\hat{\lambda}_{l,j}^{e,s}$ are the dual variables with respect to constraints in (26b). From the conditions above, the optimal $\hat{\mathbf{s}}$ can be derived as

$$\hat{\mathbf{s}}=\left(\left(2\rho+2\lambda\right)\mathbf{I}_{N_tL}-2\hat{\mathbf{B}}+\rho\mathbf{T}\right)^{-1}\mathbf{y}, \tag{36}$$

where

$$\begin{aligned}\mathbf{T}=&\sum_{l,k}\left(\tilde{\mathbf{f}}_{l,k}\left(\boldsymbol{\Theta}_t\right)\tilde{\mathbf{f}}_{l,k}^{T}\left(\boldsymbol{\Theta}_t\right)+\hat{\mathbf{f}}_{l,k}\left(\boldsymbol{\Theta}_t\right)\hat{\mathbf{f}}_{l,k}^{T}\left(\boldsymbol{\Theta}_t\right)\right)\\&+\sum_{l,j}\left(\tilde{\mathbf{t}}_{l,j}\left(\boldsymbol{\Theta}_t\right)\tilde{\mathbf{t}}_{l,j}^{T}\left(\boldsymbol{\Theta}_t\right)+\hat{\mathbf{t}}_{l,j}\left(\boldsymbol{\Theta}_t\right)\hat{\mathbf{t}}_{l,j}^{T}\left(\boldsymbol{\Theta}_t\right)\right),\end{aligned} \tag{37}$$

$$\begin{aligned}\mathbf{y}=&\rho\left(\sum_{l,k}\left(\tilde{\mathbf{f}}_{l,k}\left(\boldsymbol{\Theta}_t\right)\tilde{r}_{u_k}+\hat{\mathbf{t}}_{l,k}\left(\boldsymbol{\Theta}_t\right)\hat{r}_{u_k}\right)+\breve{\mathbf{s}}\right)\\&+\rho\left(\sum_{l,j}\left(\tilde{\mathbf{t}}_{l,j}\left(\boldsymbol{\Theta}_t\right)\tilde{\eta}_{e_j}+\hat{\mathbf{t}}_{l,j}\left(\boldsymbol{\Theta}_t\right)\hat{\eta}_{e_j}\right)+\bar{\mathbf{s}}\right)+2\lambda\mathbf{s}_0,\end{aligned}$$

where λ can be obtained using the bisection search method to satisfy condition (31).

Algorithm 1 summarizes the proposed distance-majorization induced iterative algorithm for optimizing the transmission signal $\hat{\mathbf{s}}$.

Theorem 2: Define $\tilde{c}_{l,k}^{u}\left(\hat{\mathbf{s}}^*\right)\triangleq\text{dist}\left(\tilde{\mathbf{f}}_{l,k}^{H}\left(\boldsymbol{\Theta}_t\right)\hat{\mathbf{s}}^*,\Xi\right)$, $\hat{c}_{l,k}^{u}\left(\hat{\mathbf{s}}^*\right)\triangleq\text{dist}\left(\hat{\mathbf{f}}_{l,k}^{H}\left(\boldsymbol{\Theta}_t\right)\hat{\mathbf{s}}^*,\Xi\right)$, $\hat{c}_{l,j}^{e}\left(\hat{\mathbf{s}}^*\right)\triangleq\text{dist}\left(\hat{\mathbf{t}}_{l,j}^{H}\left(\boldsymbol{\Theta}_r\right)\hat{\mathbf{s}}^*,\Psi\right)$, $\tilde{c}_{l,j}^{e}\left(\hat{\mathbf{s}}^*\right)\triangleq\text{dist}\left(\tilde{\mathbf{t}}_{l,j}^{H}\left(\boldsymbol{\Theta}_r\right)\hat{\mathbf{s}}^*,\Psi\right)$, and $c\left(\hat{\mathbf{s}}^*\right)\triangleq\text{dist}\left(\hat{\mathbf{s}}^*,\Omega\right)$, $k\in\mathcal{K}_u$, $j\in\mathcal{K}_e$, $l\in\mathcal{L}$. Suppose that a limit solution $\mathbf{s}$ obtained with Algorithm 1 makes $\Upsilon\left(\mathbf{s},\breve{\beta}\right)\triangleq-2\hat{\mathbf{B}}\hat{\mathbf{s}}^*+2\breve{\lambda}\left(\hat{\mathbf{s}}^*-\hat{\mathbf{s}}_0\right)+\rho\sum_{l,k}\tilde{c}_{l,k}^{u}\left(\hat{\mathbf{s}}^*\right)\nabla\tilde{c}_{l,k}^{u}\left(\hat{\mathbf{s}}^*\right)+\rho\sum_{l,k}\hat{c}_{l,k}^{u}\left(\hat{\mathbf{s}}^*\right)\nabla\hat{c}_{l,k}^{u}\left(\hat{\mathbf{s}}^*\right)+\rho\sum_{l,k}\hat{c}_{l,k}^{e}\left(\hat{\mathbf{s}}^*\right)\nabla\hat{c}_{l,k}^{e}\left(\hat{\mathbf{s}}^*\right)+\rho\sum_{l,k}\tilde{c}_{l,k}^{e}\left(\hat{\mathbf{s}}^*\right)\nabla\tilde{c}_{l,k}^{e}\left(\hat{\mathbf{s}}^*\right)+2c\left(\hat{\mathbf{s}}^*\right)\nabla c\left(\hat{\mathbf{s}}^*\right)\rightarrow0$ as $\rho\rightarrow+\infty$, where $\breve{\lambda}$ is Lagrange multiplier associated with the inequality constraint in (26b). Besides, if $\hat{\mathbf{s}}^*$ is feasible and the gradients $\nabla\hat{c}_{l,k}^{u}\left(\hat{\mathbf{s}}^*\right)$, $\nabla\tilde{c}_{l,k}^{u}\left(\hat{\mathbf{s}}^*\right)$, $\nabla\hat{c}_{l,k}^{e}\left(\hat{\mathbf{s}}^*\right)$, $\nabla\tilde{c}_{l,k}^{e}\left(\hat{\mathbf{s}}^*\right)$, and $\nabla c\left(\hat{\mathbf{s}}^*\right)$ are linearly independent, the convergent solution $\hat{\mathbf{s}}^*$ is a Karush-Kuhn-Tucker (KKT) solution of problem (21).

Proof: The proof is given in Appendix C. ■

Remark 2: The approach for selecting and updating the penalty parameter ρ is crucial for our proposed distance-majorization algorithm [65, Charpter 17]. For designing an efficient algorithm, we follow existing works adopting the penalty approach, e.g. [61, Algorithm 1], [66, Algorithm 1], to use the classical penalty method given in [65, Framework 17.2], which initializes ρ with a small value and increases it gradually until feasibility is attained. The efficiency of the updating strategy has been validated by existing works [61], [66].

Algorithm 1 Proposed Distance-Majorization Algorithm for Solving Problem (21)

1: Initialize $\rho=1$, $c=2$, $T=30$, $\rho_{\max}\gg1$, $\hat{\mathbf{s}}(1)=\hat{\mathbf{s}}(0)\in\mathbb{R}^{2N_tL\times1}$, the convergence tolerance $\epsilon\ll1$, and $m=1$.
2: **Repeat**
3: $\hat{\mathbf{z}}(m)=\hat{\mathbf{s}}(m)+\frac{m-1}{m+2}\left(\hat{\mathbf{s}}(m)-\hat{\mathbf{s}}(m-1)\right)$,
4: Project $\hat{\mathbf{z}}(m)$ on the sets defined by (21a), (21b), and (21c) and obtain $\tilde{\gamma}_{u,k}$, $\hat{\gamma}_{u,k}$, $\tilde{\eta}_{e,k}$, and $\hat{\eta}_{e,k}$, $k\in\mathcal{K}_u$, $k\in\mathcal{K}_e$, $l\in\mathcal{L}$.
5: Obtain $\hat{\mathbf{s}}$ with (36),
6: Update $\rho=\min\left(\rho_{\max},c\rho\right)$, every T iterations
7: $m=m+1$,
8: **Until** $||\mathbf{s}(m+1)-\mathbf{s}(m)||_2\leq\epsilon$.

B. Optimization of $\boldsymbol{\Theta}_t$ and $\boldsymbol{\Theta}_r$

In this subsection, we study the joint optimization of $\boldsymbol{\Theta}_t$ and $\boldsymbol{\Theta}_r$ for the second subproblem in AO. Before proceeding, we first perform some equivalent transformations. In particular, by employing [50, eq. (1.11.18)], we have

$$\begin{aligned}\tilde{\mathbf{h}}_{l,k}^{H}\left(\boldsymbol{\Theta}_t\right)\mathbf{s}&=\tilde{\beta}_{l,k}\text{vec}\left(\mathbf{h}_{u_k}^{H}\boldsymbol{\Theta}_t\mathbf{G}\mathbf{s}\mathbf{e}_{l,L}\right)\\&=\tilde{\beta}_{l,k}\left(\left(\mathbf{G}\mathbf{s}\mathbf{e}_{l,L}\right)^{T}\otimes\mathbf{h}_{u_k}^{H}\right)\text{vec}\left(\boldsymbol{\Theta}_t\right)\\&\overset{(a)}{=}\tilde{\beta}_{l,k}\left(\left(\mathbf{G}\mathbf{S}\mathbf{e}_{l,L}\right)^{T}\otimes\mathbf{h}_{u_k}^{H}\right)\mathbf{L}_d\boldsymbol{\theta}_t,\end{aligned} \tag{38}$$

where step (a) is obtained according to [67, eq. (2.42)] and $\mathbf{L}_d$ is defined by [67, Definition 2.12]. Furthermore, by employing the vectorization operator given in [50, Section 1.11.2], the objective function in (18a) can be reformulated as

$$\sum_{i=1}^{M}P(\theta_i,\psi_i)=\boldsymbol{\theta}_r^{H}\mathbf{Q}\boldsymbol{\theta}_r+2\mathcal{R}\left(\mathbf{q}^{H}\boldsymbol{\theta}_r\right)+p, \tag{39}$$

where $\mathbf{Q}\triangleq\sum_{i=1}^{M}\mathbf{L}_d^{H}\left(\left(\mathbf{G}\mathbf{S}\mathbf{S}^{H}\mathbf{G}^{H}\right)^{T}\otimes\left(\mathbf{a}_N(\theta_i)\mathbf{a}_N^{H}(\theta_i)\right)\right)\mathbf{L}_d$, $\mathbf{q}=\sum_{i=1}^{M}\mathbf{L}_d^{H}\text{vec}\left(\mathbf{a}_N(\theta_i)\mathbf{a}_{N_t}^{H}(\psi_i)\mathbf{S}\mathbf{S}^{H}\mathbf{G}^{H}\right)$, and $p=\sum_{i=1}^{M}\mathbf{a}_{N_t}^{H}(\psi_i)\mathbf{S}\mathbf{S}^{H}\mathbf{a}_{N_t}(\psi_i)$.

Based on the above reformulations, the joint optimization

of $\mathbf{\Theta}_t$ and $\mathbf{\Theta}_r$ can be formulated as

$$\begin{aligned}
&\underset{\boldsymbol{\theta}_r,\boldsymbol{\theta}_t}{\text{maximize}}\ \boldsymbol{\theta}_r^H\mathbf{Q}\boldsymbol{\theta}_r+2\mathcal{R}\left(\mathbf{q}^H\boldsymbol{\theta}_r\right)\\
&\text{s.t.}\mathcal{R}\left(-\tilde{\beta}_{l,k}\left(\left(\mathbf{GSe}_{l,L}\right)^T\otimes\mathbf{h}_{u_k}^H\right)\mathbf{L}_d\boldsymbol{\theta}_t\right)\le-\gamma_{u_k},\\
&\quad l\in\mathcal{L},\ k\in\mathcal{K}_u, &(40a)\\
&\quad\mathcal{R}\left(-\hat{\beta}_{l,k}\left(\left(\mathbf{GSe}_{l,L}\right)^T\otimes\mathbf{h}_{u_k}^H\right)\mathbf{L}_d\boldsymbol{\theta}_t\right)\le-\gamma_{u_k},\\
&\quad l\in\mathcal{L},\ k\in\mathcal{K}_u, &(40b)\\
&\quad\mathcal{R}\left(-\tilde{\alpha}_{l,\hat{u}}\left(\left(\mathbf{GSe}_{l,L}\right)^T\otimes\mathbf{g}_{e_k}^H\right)\mathbf{L}_d\boldsymbol{\theta}_r\right)\le-\eta_{e_k}\\
&\quad+\mathcal{R}\left(\tilde{\alpha}_{l,\hat{u}}\left(\mathbf{e}_{l,L}^T\otimes\mathbf{t}_{e_k}^H\right)\mathbf{s}\right),\ l\in\mathcal{L},k\in\mathcal{K}_e, &(40c)\\
&\quad\mathcal{R}\left(-\hat{\alpha}_{l,\hat{u}}\left(\left(\mathbf{GSe}_{l,L}\right)^T\otimes\mathbf{g}_{e_k}^H\right)\mathbf{L}_d\boldsymbol{\theta}_r\right)\le-\eta_{e_k}\\
&\quad+\mathcal{R}\left(\hat{\alpha}_{l,\hat{u}}\left(\mathbf{e}_{l,L}^T\otimes\mathbf{t}_{e_k}^H\right)\mathbf{s}\right),\ l\in\mathcal{L},k\in\mathcal{K}_e, &(40d)\\
&\quad[\boldsymbol{\theta}_r]_n^2+[\boldsymbol{\theta}_t]_n^2=1,\ 1\le n\le N, &(40e)
\end{aligned}$$

where

$$\tilde{\beta}_{l,k}\triangleq e^{-j\angle x_k(l)}\left(\sin(\Phi)+e^{-j\frac{\pi}{2}}\cos(\Phi)\right), \quad (41)$$

$$\hat{\beta}_{l,k}\triangleq e^{-j\angle x_k(l)}\left(\sin(\Phi)-e^{-j\frac{\pi}{2}}\cos(\Phi)\right), \quad (42)$$

$$\tilde{\alpha}_{l,\hat{u}}\triangleq e^{-j\angle s_{\hat{u}}(l)}\left(\sin(\Phi)+e^{-j\frac{\pi}{2}}\cos(\Phi)\right), \quad (43)$$

$$\hat{\alpha}_{l,\hat{u}}\triangleq e^{-j\angle s_{\hat{u}}(l)}\left(\sin(\Phi)-e^{-j\frac{\pi}{2}}\cos(\Phi)\right). \quad (44)$$

To facilitate the algorithm design, using (20), we first reformulate problem (40) as its real-valued counterpart given by

$$\begin{aligned}
&\underset{\hat{\boldsymbol{\theta}}_r,\hat{\boldsymbol{\theta}}_t}{\text{maximize}}\ \hat{\boldsymbol{\theta}}_r^T\bar{\mathbf{Q}}\hat{\boldsymbol{\theta}}_r+2\bar{\mathbf{q}}^T\hat{\boldsymbol{\theta}}_r &(45a)\\
&\text{s.t.}\tilde{\mathbf{v}}_{l,k}\hat{\boldsymbol{\theta}}_t\le-\gamma_{u_k},\ \hat{\mathbf{v}}_{l,k}\hat{\boldsymbol{\theta}}_t\le-\gamma_{u_k},\ k\in\mathcal{K}_u,\ l\in\mathcal{L}, &(45b)\\
&\quad\tilde{\mathbf{p}}_{l,k}\hat{\boldsymbol{\theta}}_r\le-\tilde{\eta}_{e,l,k},\ \hat{\mathbf{p}}_{l,k}\hat{\boldsymbol{\theta}}_r\le-\hat{\eta}_{e,l,k},\ k\in\mathcal{K}_e,\ l\in\mathcal{L}, &(45c)\\
&\quad[\hat{\boldsymbol{\theta}}_r]_n^2+[\hat{\boldsymbol{\theta}}_r]_{n+N}^2+[\hat{\boldsymbol{\theta}}_t]_n^2+[\hat{\boldsymbol{\theta}}_t]_{n+N}^2=1,\ 1\le n\le N, &(45d)
\end{aligned}$$

where $\mathbf{v}_{l,k}\triangleq\left(\left(\mathbf{GSe}_{l,L}\right)^T\otimes\mathbf{h}_{u_k}^H\right)\mathbf{L}_d$, $\mathbf{p}_{l,k}\triangleq\left(\left(\mathbf{GSe}_{l,L}\right)^T\otimes\mathbf{g}_{e_k}^H\right)\mathbf{L}_d$, $-\tilde{\eta}_{e,l,k}=-\eta_{e_k}+\mathcal{R}\left(\tilde{\alpha}_{l,\hat{u}}\left(\mathbf{e}_{l,L}^T\otimes\mathbf{t}_{e_k}^H\right)\mathbf{s}\right)$, $-\hat{\eta}_{e,l,k}=-\eta_{e_k}+\mathcal{R}\left(\hat{\alpha}_{l,\hat{u}}\left(\mathbf{e}_{l,L}^T\otimes\mathbf{t}_{e_k}^H\right)\mathbf{s}\right)$, and

$$\bar{\mathbf{Q}}=\begin{bmatrix}\mathcal{R}(\mathbf{Q}), & -\mathcal{I}(\mathbf{Q})\\ \mathcal{I}(\mathbf{Q}), & \mathcal{R}(\mathbf{Q})\end{bmatrix},\ \bar{\mathbf{q}}=\left[\mathcal{R}(\mathbf{q}),-\mathcal{I}(\mathbf{q})\right]^T, \quad (46)$$

$$\hat{\boldsymbol{\theta}}_t\triangleq\left[\mathcal{R}(\boldsymbol{\theta}_t),\mathcal{I}(\boldsymbol{\theta}_t)\right],\ \hat{\boldsymbol{\theta}}_r\triangleq\left[\mathcal{R}(\boldsymbol{\theta}_r),\mathcal{I}(\boldsymbol{\theta}_r)\right] \quad (47)$$

$$\tilde{\mathbf{v}}_{l,k}\triangleq\left[\mathcal{R}\left(-\tilde{\beta}_{l,k}\mathbf{v}_{l,k}\right),\mathcal{I}\left(\tilde{\beta}_{l,k}\mathbf{v}_{l,k}\right)\right], \quad (48)$$

$$\hat{\mathbf{v}}_{l,k}\triangleq\left[\mathcal{R}\left(-\hat{\beta}_{l,k}\mathbf{v}_{l,k}\right),\mathcal{I}\left(\hat{\beta}_{l,k}\mathbf{v}_{l,k}\right)\right], \quad (49)$$

$$\tilde{\mathbf{p}}_{l,k}\triangleq\left[\mathcal{R}\left(-\tilde{\alpha}_{l,\hat{u}}\mathbf{p}_{l,k}\right),\mathcal{I}\left(\tilde{\alpha}_{l,\hat{u}}\mathbf{p}_{l,k}\right)\right], \quad (50)$$

$$\hat{\mathbf{p}}_{l,k}\triangleq\left[\mathcal{R}\left(-\hat{\alpha}_{l,\hat{u}}\mathbf{p}_{l,k}\right),\mathcal{I}\left(\hat{\alpha}_{l,\hat{u}}\mathbf{p}_{l,k}\right)\right]. \quad (51)$$

Since problem (45) is nonconvex due to the objective function in (45a) and constraint (45d), it is challenging to solve problem (45) directly. Besides, even if the nonconvexity is not considered, the computational complexity of solving problem (45) with the interior point method is very high due to the involved $2(K_u+K_e)L$ affine constraints, namely (45b)-(45d).

Taking these considerations into account, we again apply the distance-majorization algorithm to handle problem (45). Firstly, with the Courant's penalty method [60], an equivalent problem with an augmented objective function can be formulated as follows

$$\underset{\boldsymbol{\theta},\tilde{z}_{l,k},\hat{z}_{l,k},\tilde{x}_{l,k},\hat{x}_{l,k}}{\text{minimize}}\ -\boldsymbol{\theta}^T\mathbf{E}_r\bar{\mathbf{Q}}\mathbf{E}_r^T\boldsymbol{\theta}-2\bar{\mathbf{q}}^T\mathbf{E}_r^T\boldsymbol{\theta}+\frac{\rho}{2}\mathrm{dist}^2\left(\boldsymbol{\varpi},\Theta\right) \quad (52a)$$

$$\text{s.t. }\tilde{z}_{l,k}=\tilde{\mathbf{v}}_{l,k}\mathbf{E}_t^T\boldsymbol{\theta},\ \hat{z}_{l,k}=\hat{\mathbf{v}}_{l,k}\mathbf{E}_t^T\boldsymbol{\theta}, \quad (52b)$$

$$\tilde{x}_{l,k}=\tilde{\mathbf{p}}_{l,k}\mathbf{E}_r^T\boldsymbol{\theta},\ \hat{x}_{l,k}=\hat{\mathbf{p}}_{l,k}\mathbf{E}_r^T\boldsymbol{\theta}, \quad (52c)$$

where $\mathbf{E}_t=[\mathbf{I}_{2N};\mathbf{0}_{2N}]$, $\mathbf{E}_r=[\mathbf{0}_{2N};\mathbf{I}_{2N}]$, $\boldsymbol{\varpi}\triangleq\{\boldsymbol{\theta},\tilde{z}_{l,k},\hat{z}_{l,k},\tilde{x}_{l,k},\hat{x}_{l,k}\}$, and Θ is the feasible set spanned by (45b)-(45d).

Following the proof of Theorem 1, it can be easily proved that the optimal solution of problem (52) is also the optimal solution of problem (45). However, problem (52) is still challenging to solve, since calculating $\mathrm{dist}^2\left(\boldsymbol{\varpi},\Theta\right)$ involves solving a high-dimensional convex optimization problem and the objective function is still nonconvex. Therefore, similar to handling problem (26), we propose an MM-based iterative algorithm to handle problem (52) and a surrogate function of the objective function (52a) can be written as

$$\begin{aligned}
G(\boldsymbol{\theta})\triangleq&-\boldsymbol{\theta}^T\mathbf{E}_r\bar{\mathbf{Q}}\mathbf{E}_r^T\boldsymbol{\theta}-2\bar{\mathbf{q}}^T\mathbf{E}_r^T\boldsymbol{\theta}+\frac{\rho}{2}\sum_{l,k}|\tilde{z}_{l,k}-\tilde{r}_{u_k}|^2\\
&+\frac{\rho}{2}\sum_{l,k}|\hat{z}_{l,k}-\hat{r}_{u_k}|^2+\frac{\rho}{2}\sum_{l,i}|\tilde{x}_{l,k}-\tilde{r}_{e_k}|^2+\frac{\rho}{2}\sum_{l,k}|\hat{x}_{l,k}-\hat{r}_{e_k}|^2\\
&+\frac{\rho}{2}\left(||\mathbf{E}_t^T\boldsymbol{\theta}-\hat{\boldsymbol{\theta}}_t||_2^2\right)+\frac{\rho}{2}\left(||\mathbf{E}_r^T\boldsymbol{\theta}-\hat{\boldsymbol{\theta}}_r||_2^2\right), \quad (53)
\end{aligned}$$

where $\tilde{r}_{u_k}$, $\hat{r}_{u_k}$, $\tilde{r}_{e_k}$, $\hat{r}_{e_k}$, $\hat{\boldsymbol{\theta}}_t$, and $\hat{\boldsymbol{\theta}}_r$ are the solutions obtained by projecting $\tilde{z}_{l,i}$, $\hat{z}_{l,i}$, $\tilde{x}_{l,k}$, $\hat{x}_{l,k}$, $\mathbf{E}_t^T\boldsymbol{\theta}$, and $\mathbf{E}_r^T\boldsymbol{\theta}$ onto the feasible sets defined by (45b)-(45d). However, $G(\boldsymbol{\theta})$ is still a nonconvex function. Then, we exploit the strong duality of the nonconvex quadratic problem [64] and introduce a quadratic constraint to formulate the following problem of minimizing a nonconvex quadratic function over a Euclidean ball, i.e.,

$$\begin{aligned}
&\underset{\boldsymbol{\theta}}{\text{minimize}}\ G(\boldsymbol{\theta}) &(54a)\\
&\text{s.t. }\boldsymbol{\theta}^T\boldsymbol{\theta}\le N, &(54b)\\
&\quad\tilde{z}_{l,k}=\tilde{\mathbf{v}}_{l,k}\mathbf{E}_t^T\boldsymbol{\theta},\ \hat{z}_{l,k}=\hat{\mathbf{v}}_{l,k}\mathbf{E}_t^T\boldsymbol{\theta}, &(54c)\\
&\quad\tilde{x}_{l,k}=\tilde{\mathbf{p}}_{l,k}\mathbf{E}_r^T\boldsymbol{\theta},\ \hat{x}_{l,k}=\hat{\mathbf{p}}_{l,k}\mathbf{E}_r^T\boldsymbol{\theta}. &(54d)
\end{aligned}$$

It is worth noting that the additional constraint (54b) does not shrink the feasible set of problem (54) due to constraint (45d).

Although problem (54) is nonconvex, its optimal solution still satisfies the following KKT condition that is given by

$$\begin{aligned}
&-2\mathbf{E}_r\bar{\mathbf{Q}}\mathbf{E}_r^T\boldsymbol{\theta}-2\mathbf{E}_r\mathbf{q}+\rho\mathbf{E}_t\left(\mathbf{E}_t^T\boldsymbol{\theta}-\hat{\boldsymbol{\theta}}_t\right)\\
&+\rho\mathbf{E}_r\left(\mathbf{E}_r^T\boldsymbol{\theta}-\hat{\boldsymbol{\theta}}_r\right)+\sum_{l,k}\tilde{u}_{l,k}\mathbf{E}_t\tilde{\mathbf{v}}_{l,k}^T+\sum_{l,k}\hat{u}_{l,k}\mathbf{E}_t\hat{\mathbf{v}}_{l,k}^T\\
&+\sum_{l,k}\tilde{\nu}_{l,k}\mathbf{E}_r\tilde{\mathbf{p}}_{l,k}^T+\sum_{l,k}\tilde{\nu}_{l,k}\mathbf{E}_r\tilde{\mathbf{p}}_{l,k}^T=\mathbf{0}, \quad (55)\\
&\rho\left(\tilde{z}_{l,k}-\tilde{r}_{u_k}\right)-\tilde{u}_{l,k}=0,\quad\rho\left(\hat{z}_{l,k}-\hat{r}_{u_k}\right)-\hat{u}_{l,k}=0, \quad (56)\\
&\rho\left(\tilde{x}_{l,k}-\tilde{r}_{e_k}\right)-\tilde{x}_{l,k}=0,\quad\rho\left(\hat{x}_{l,k}-\hat{r}_{e_k}\right)-\hat{x}_{l,k}=0. \quad (57)
\end{aligned}$$

Then, from the KKT conditions above, the optimal solution

Algorithm 2 Proposed Distance-Majorization Algorithm for Solving Problem (40)

1: Initialize $\rho = 1$, $c = 2$, $T = 30$, $\rho_{\max} \gg 1$, $\boldsymbol{\theta}(1) = \boldsymbol{\theta}(0) \in \mathbb{R}^{4N\times 1}$, the convergence tolerance $\epsilon \ll 1$, and $k = 1$.
2: **Repeat**
3: $\mathbf{y}(k) = \boldsymbol{\theta}(k) + \frac{k-1}{k+2}\left(\boldsymbol{\theta}(k) - \boldsymbol{\theta}(k-1)\right)$,
4: Project $\mathbf{y}(k)$ on the sets defined by (45b)-(45d), and obtain $\hat{\boldsymbol{\theta}}_t$, $\hat{\boldsymbol{\theta}}_r$, $\hat{\gamma}_{u_k}$, $\hat{\gamma}_{u_k}$, $\hat{r}_{e_k}$, and $\hat{r}_{e_k}$, $k \in \mathcal{K}_u$, $k \in \mathcal{K}_e$, $l \in \mathcal{L}$.
5: Obtain $\boldsymbol{\theta}$ with (58),
6: Update $\rho = \min\left(\rho_{\max}, c\rho\right)$, every T iterations
7: $k = k + 1$,
8: **Until** $||\boldsymbol{\theta}(k+1) - \boldsymbol{\theta}(k)||_2 \leq \epsilon$.

Algorithm 3 Proposed AO Algorithm for the Joint Optimization of $\mathbf{S}$, $\boldsymbol{\Theta}_t$, and $\boldsymbol{\Theta}_r$

1: Initialize the convergence tolerance $\breve{\epsilon} = 10^{-1}$,
2: **Repeat**
3: Optimize $\mathbf{S}$ with Algorithm 1,
4: Optimize $\boldsymbol{\Theta}_t$ and $\boldsymbol{\Theta}_r$ with Algorithm 2,
5: **Until** the increase of the objective function is smaller than $\breve{\epsilon}$.

of problem (54) can be derived as

$$\boldsymbol{\theta} = \mathbf{M}^{-1}\mathbf{N}, \tag{58}$$

where

$$\begin{aligned}
\mathbf{M} \triangleq\ & -2\bar{\mathbf{Q}}\mathbf{E}_r^T + \rho\mathbf{E}_t\mathbf{E}_t^T + \rho\mathbf{E}_r\mathbf{E}_r^T + \rho\sum_{l,k}\mathbf{E}_t\tilde{\mathbf{v}}_{l,k}^T\tilde{\mathbf{v}}_{l,k}\mathbf{E}_t^T \\
& + \rho\sum_{l,k}\mathbf{E}_t\hat{\mathbf{v}}_{l,k}^T\hat{\mathbf{v}}_{l,k}\mathbf{E}_t^T + \rho\sum_{l,k}\mathbf{E}_r\tilde{\mathbf{p}}_{l,k}^T\tilde{\mathbf{p}}_{l,k}\mathbf{E}_r^T \\
& + \rho\sum_{l,k}\mathbf{E}_r\hat{\mathbf{p}}_{l,k}^T\hat{\mathbf{p}}_{l,k}\mathbf{E}_r^T + 2\lambda\mathbf{I}_{4N}, \\
\mathbf{N} \triangleq\ & 2\mathbf{E}_r\bar{\mathbf{q}} + \rho\sum_{l,k}\mathbf{E}_t\tilde{\mathbf{v}}_{l,k}^T\tilde{r}_{u_k} + \rho\sum_{l,k}\mathbf{E}_t\hat{\mathbf{v}}_{l,k}^T\hat{r}_{u_k} \\
& \rho\sum_{l,k}\mathbf{E}_r\tilde{\mathbf{p}}_{l,k}^T\tilde{r}_{e,l,k} + \rho\sum_{l,k}\mathbf{E}_r\hat{\mathbf{p}}_{l,k}^T\hat{r}_{e,l,k} + \rho\mathbf{E}_r\hat{\boldsymbol{\theta}}_r + \rho\mathbf{E}_t\hat{\boldsymbol{\theta}}_t.
\end{aligned}$$

Algorithm 2 summarizes the proposed distance-majorization induced iterative algorithm for optimizing the transmit and reflective beamforming matrices. Similarly, Algorithm 2 can also be proved to converge to the KKT solution of problem (40).

Finally, Algorithm 3 summarizes the proposed AO-based iterative algorithm for handling the joint optimization of $\mathbf{S}$, $\boldsymbol{\Theta}_t$, and $\boldsymbol{\Theta}_r$. Since Algorithm 1 and Algorithm 2 can be proved to obtain KKT solutions of the subproblems in Algorithm 3, the objective function certainly increases during the iteration. This has been validated by simulation results in Fig. 3. Then, we can conclude that the convergence of Algorithm 3 can be guaranteed due to the limited power budget.

C. Computational Complexity Analysis

The computational complexity of Algorithm 3 is dominated by calculating the required matrix inversion in (36) and (58). Since $\mathbf{B}$ and $\mathbf{T}$ are both block diagonal matrices, the computational complexity of calculating (36) is $\mathcal{O}\left(LN_t^{2.373}\right)$ [59]. Similarly, $\mathbf{M}$ is also a block diagonal matrix and the computational complexity of calculating (58) is $\mathcal{O}\left(N^{2.373}\right)$. Therefore, the computational complexity of Algorithm 3 is dominated by $\mathcal{O}\left(L\left(\mathrm{I}_{\mathbf{s}}N_t^{2.373} + \mathrm{I}_{\boldsymbol{\theta}}N^{2.373}\right)\right)$, where $\mathrm{I}_{\mathbf{s}}$ and $\mathrm{I}_{\boldsymbol{\theta}}$ are the number of iterations needed to calculate (36) and (58) in Algorithm 3. In contrast, the computational complexity of ADMM algorithm in Appendix A is $\hat{\mathrm{I}}_{\mathbf{s}}\mathcal{O}(1)N_{\mathbf{s}} + \hat{\mathrm{I}}_{\boldsymbol{\theta}}\mathcal{O}(1)N_{\boldsymbol{\theta}}$, where $N_{\mathbf{s}} \triangleq \mathcal{O}(1)\left(2(K_u+K_e)L + N_tL + 1\right)^{\frac{1}{2}} N_tL\left((N_tL)^2 + 2(K_u+K_e)L + 2N_tL\right)$ and $N_{\boldsymbol{\theta}} \triangleq \mathcal{O}(1)\left(2(K_u+K_e)L+1\right)^{\frac{1}{2}} 4N\left((4N)^2 + 2(K_u+K_e)L\right)$ [59]. And $\hat{\mathrm{I}}_{\mathbf{s}}$ and $\hat{\mathrm{I}}_{\boldsymbol{\theta}}$ denote the number of iterations for optimizing $\mathbf{s}$ and $\boldsymbol{\theta}$ with ADMM. Therefore, our proposed distance-majorization induced iterative algorithm has a much lower computational complexity, especially for a large L.

IV. Simulation Results

In this section, we adopt Monte Carlo simulations to evaluate the performance of our proposed distance-majorization induced iterative algorithm. The locations of the BS and the STAR-RIS are $(0\text{ m}, 0\text{ m})$ and $(30\text{ m}, 30\text{ m})$, respectively. The number of users and targets are $K_u = 2$ and $K_e = 3$ respectively, whose locations are generated uniformly in the region of $[0, 100\text{ m}] \times [0, 100\text{ m}]$. In particular, the random locations of the users are $(88.1120\text{ m}, 39.2204\text{ m})$ and $(92.1621\text{ m}, 27.6774\text{ m})$. The locations of the malicious targets are generated randomly in the two-dimensional annulus formed by two concentric circles centered at the origin, whose inner diameter is 50 m and outer diameter is 70 m. Similar to [13], we model the path loss as $35.3 + 37.6\log_{10}l_{\text{ab}}$ (dB), where l_{ab} is the transmission distance from a to b. Unless specified otherwise, the noise power σ^2 is -100 dBm/Hz, the PAPR $\eta = 2.2$, and the Rician factor is 5 dB. Besides, following [18], [46], we adopt the orthogonal linear frequency modulation (LFM) as the reference waveform which enjoys good pulse compression and ambiguity properties that facilitate the detection of point targets. The (k,q)th entry of $\mathbf{S}_0$ is $\mathbf{S}_0(k,q) = \sqrt{\frac{P_t}{N_tL}}e^{\frac{j2\pi k(q-1)}{L}}e^{\frac{j2\pi(q-1)^2}{L}}$ [47]. Then, we set the reference waveform in problem (18) as $\mathbf{s}_0 = \text{vec}\left(\mathbf{S}_0\right)$. To validate the efficiency of our proposed distance-majorization induced low-complexity algorithm (DMLCA) in Algorithm 3, following [18], we employ the ADMM algorithm to introduce the benchmark algorithm given in Appendix A.

Fig. 3 shows the convergence rate of our proposed DMLCA in Algorithm 3, which includes the average radar sensing power achieved by optimizing $\mathbf{S}$ and $(\boldsymbol{\Theta}_r, \boldsymbol{\Theta}_t)$ alternately. Clearly, the convergence rate of the proposed DMLCA is fast, which validates its efficiency. Besides, DMLCA has a similar convergence performance for different values of N, which validates its practicability and shows that DMLCA enjoys an excellent scalability.

Fig. 4 shows the performance comparison between DMLCA and the ADMM-based algorithm. Considering the high computational complexity of ADMM when L is large, we set $L = 1$ to facilitate the performance comparison. Clearly,

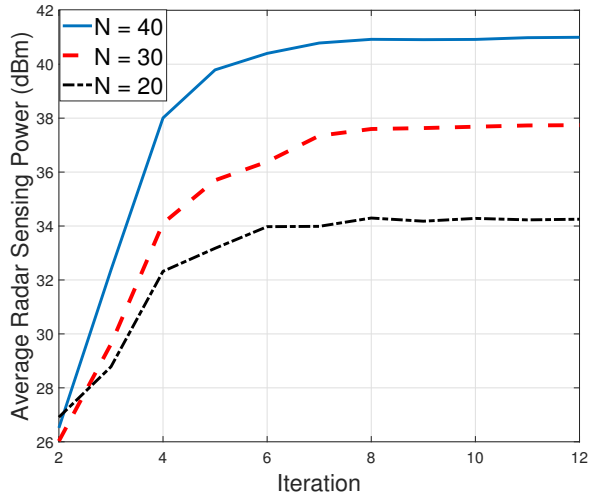

Fig. 3. Convergence of our proposed DMLCA with $N_t = 12$, $K_u = 2$, $K_e = 3$, $P_t = 40$ dBm, $L = 20$, $\epsilon = 0.2$, and different N.

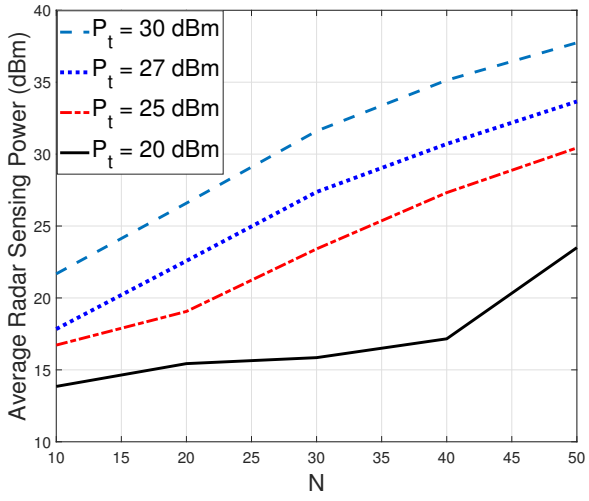

Fig. 5. Average radar sensing power versus the increasing N with $N_t = 12$, $N = 20$, $K_u = 2$, $K_e = 3$, $\epsilon = 1.2$, and $L = 10$.

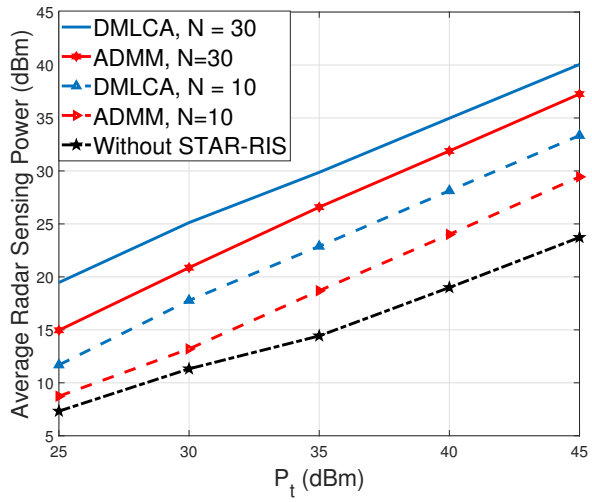

Fig. 4. Performance comparison between our DMLCA and ADMM-based algorithm for different N with $N_t = 12$, $K_u = 2$, $K_e = 3$, $\epsilon = 0.8$, and $L = 1$.

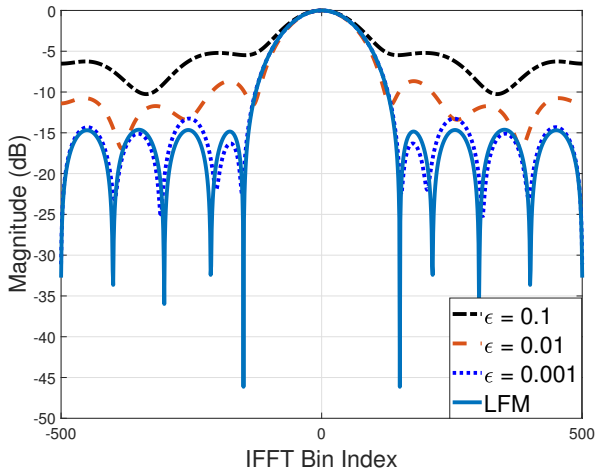

Fig. 6. Pulse compression profile of the signal waveform for different similarity constraints ϵ with $P_{\text{tot}} = 20$ dBm, $N = 20$, $N_t = 12$, $K_u = 2$, and $K_e = 3$.

DMLCA achieves better performance than ADMM. Therefore, we can conclude that our proposed DMLCA not only enjoys a much lower complexity than that of ADMM, but also achieves better performance than the latter. Furthermore, to illustrate the benefit introduced by the STAR-RIS, we also show the DFRC performance in the absence of STAR-RIS denoted as "Without STAR-RIS", whose transmit signal $\mathbf{s}$ is optimized using Algorithm 1. From Fig. 4, we can find that the performance gain brought by STAR-RIS increases with increasing P_t. This is because with increasing power budget, more power can be radiated to the STAR-RIS for improving the radar sensing performance making STAR-RIS more critical in determining the radar sensing power. On the other hand, we can also find that the average radar sensing power increases with increasing N, which is due to the increasing spatial DoF that makes more energy-focused beamforming available.

Fig. 5 shows the average radar sensing power achieved by DMLCA versus increasing N. Increasing N would enhance the signal reflection capability of the STAR-RIS, which improves the strength of the signal received at the users and the radar sensing capability. Therefore, simulation results in Fig. 5 show that the average radar sensing power increases with the increasing N. Besides, from simulation results in Fig. 5, we can find that when P_t is large, a larger improvement of the average radar sensing power can be obtained through increasing N. This because with the increased power budget, the BS can satisfy the QoS of the communication users easily. As such, the exceeding resources in terms of transmit power and spatial DoF can be effectively exploited to steer the transmitted signal towards the radar targets for improving the sensing performance.

Fig. 6 shows the pulse compression profile of the transmit signal with different ϵ. Specifically, we utilize the signal

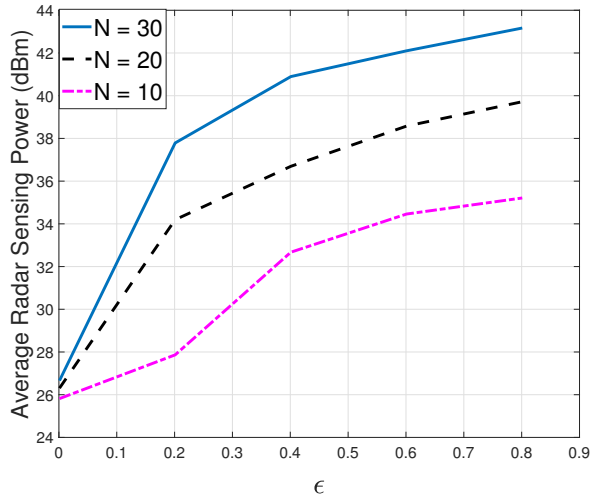

Fig. 7. Average radar sensing power versus the increasing ϵ with $N_t = 12$, $K_u = 2$, $K_e = 3$, $L = 10$, $P_t = 40$ dBm, and different N.

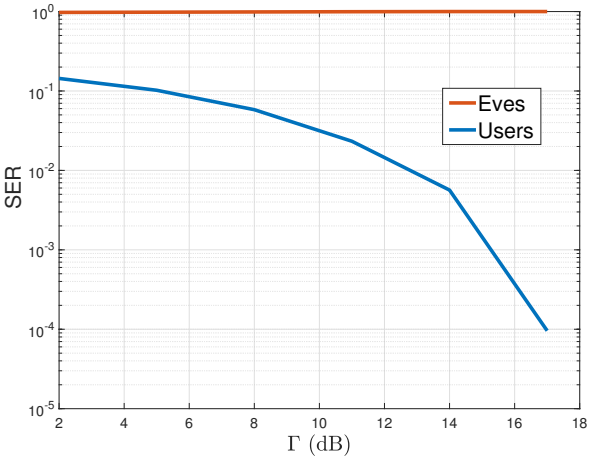

Fig. 8. Average symbol error rate (SER) versus the increasing Γ.

emitted from the first antenna to calculate the range profile. Following [47], we employ a Taylor window to perform sidelobe suppression and adopt FFT/IFFT to calculate the range profile. For comparison, the range profile of LFM is also plotted in Fig. 6. Since the increasing ϵ relaxes the similarity constraint in (18b), the range profile of the optimized signal would deviate from the required LFM gradually. Therefore, from the simulation results in Fig. 6, we can find that when $\epsilon = 0.001$, the optimized signal waveform can effectively mimic the desired LFM profile. Yet, as ϵ increases to 0.1, the difference between the range profiles of the optimized signal and LFM are enlarged. Therefore, choosing ϵ can achieve a tradeoff between the pulse compression performance and the synthetic radar sensing power, as it will be further illustrated in the following.

Fig. 7 shows the average radar sensing power versus the increasing ϵ for different N. Although increasing ϵ reduces the pulse compression performance, it enlarges the feasible set in optimizing the system resource which benefits the overall DFRC performance. Therefore, from the simulation results, we can find that the average radar sensing power increases with the increasing ϵ. Therefore, in the practical system design, the DFRC signal waveform can be designed to achieve required pulse compression performance and radar sensing power through setting ϵ as an appropriate value.

On the other hand, by setting $\Gamma_{u_k} = \Gamma_{e_n} = \Gamma$, $\forall k \in \mathcal{K}_u$, $n \in \mathcal{K}_e$ in Fig. 8, we plot the average SER versus increasing Γ. As illustrated in Fig. 2, we know that increasing Γ enhances the SINR target of multiple users and Eves, which increases the distance from the signal to the decision threshold in the signal space. Therefore, the SER of multiple users decreases with the increasing Γ. In contrast, from Fig. 8, we can find that the SER of the multiple malicious targets is almost 1 and the malicious targets have been deceived for mistaking the public signals as the confidential signals. Therefore, our proposed joint signal and reflective beamforming optimization algorithm can secure the confidential information while guaranteeing the quality of reception at multiple communication users.

V. Conclusion

We proposed a novel symbol-level precoding technique for securing the STAR-RIS-aided DFRC system, which involved the joint optimization of the transmission signal, transmission coefficients, and reflection coefficients at the STAR-RIS. Specifically, the multi-user interference is designed to be constructive to multiple legitimate users but is deceptive to Eves by restricting the signals to fall into the constructive region of the public signals. Then, the joint design was formulated as an optimization problem to maximize the radar sensing power subject to the constructive interference constraints for multiple communication users and security constraints for malicious radar targets, as well as the amplitude constraints on the transmission and reflection elements of the STAR-RIS, the PAPR constraint, and the similarity constraint between the transmitted and the reference signals. Although the considered joint optimization problem is nonconvex, we proposed a distance-majorization induced iterative algorithm to transform the nonconvex joint design problem into a sequence of subproblems, whose optimal solution in each iteration can be derived in closed-form. As confirmed by our simulation results, compared with the ADMM-induced iterative algorithm, our proposed iterative algorithm not only has a much lower computational complexity, but also achieves superior performance.

APPENDIX A
BENCHMARK ALGORITHM: ADMM-BASED JOINT OPTIMIZATION ALGORITHM

A. Optimization of $\mathbf{s}$

By introducing an auxiliary variable $\boldsymbol{\nu}$, problem (19) can be reformulated as

$$\underset{\mathbf{s},\boldsymbol{\nu},z_n}{\text{maximize}}\ \mathbf{s}^H\mathbf{B}\mathbf{s} \tag{59a}$$

$$\text{s.t. } \mathcal{R}\left(-\tilde{\mathbf{h}}_{l,k}^H\left(\boldsymbol{\Theta}_t\right)\mathbf{s}\right)\le-\gamma_{u_k},\ \mathcal{R}\left(-\hat{\mathbf{h}}_{l,k}^H\left(\boldsymbol{\Theta}_t\right)\mathbf{s}\right)\le-\gamma_{u_k},\ k\in\mathcal{K}_u,\ l\in\mathcal{L}, \tag{59b}$$

$$\mathcal{R}\left(-\tilde{\mathbf{g}}_{l,k}^H\left(\boldsymbol{\Theta}_r\right)\mathbf{s}\right)\le-\eta_{e_k},\ \mathcal{R}\left(-\hat{\mathbf{g}}_{l,k}^H\left(\boldsymbol{\Theta}_r\right)\mathbf{s}\right)\le-\eta_{e_k},\ k\in\mathcal{K}_e,\ l\in\mathcal{L}, \tag{59c}$$

$$||\mathbf{s}-\mathbf{s}_0||_2\le\sqrt{\epsilon L},\ |\mathbf{S}(i,l)|^2\le\frac{P_t\eta}{N_t},\ 1\le i\le N_t,\ l\in\mathcal{L}, \tag{59d}$$

$$||\boldsymbol{\nu}||_2^2=LP_t, \tag{59e}$$

$$\mathbf{s}=\boldsymbol{\nu}. \tag{59f}$$

Then, we apply the ADMM to handle the constant total power constraint in (59e). In particular, with the method of multipliers, its augmented Lagrangian can be formulated as

$$\underset{\mathbf{s},\boldsymbol{\nu}}{\text{maximize}}\ \mathbf{s}^H\mathbf{B}\mathbf{s}-\frac{\rho}{2}||\mathbf{s}-\boldsymbol{\nu}+\boldsymbol{\lambda}_{\mathbf{s}}||_2^2 \tag{60a}$$

$$\text{s.t. } (59b)-(59e), \tag{60b}$$

where $\boldsymbol{\lambda}_{\mathbf{s}}\succeq\mathbf{0}$ is the associated Lagrange multiplier.

With the AO, problem (60) can be decomposed into the optimization of $\mathbf{s}$ and $\boldsymbol{\nu}$. In particular, the nonconvex optimization of $\mathbf{s}$ can be achieved by employing MM.

B. Optimization of $\boldsymbol{\theta}$

By introducing auxiliary variables $\boldsymbol{\vartheta}_r$ and $\boldsymbol{\vartheta}_t$, problem (40) can be reformulated as

$$\underset{\boldsymbol{\theta}_r,\boldsymbol{\theta}_t,\boldsymbol{\vartheta}_r,\boldsymbol{\vartheta}_t}{\text{maximize}}\ \boldsymbol{\theta}_r^H\mathbf{Q}\boldsymbol{\theta}_r+2\mathcal{R}\left(\mathbf{q}^H\boldsymbol{\theta}_r\right) \tag{61a}$$

$$\text{s.t. } (45b)-(45c),\ \boldsymbol{\theta}_r=\boldsymbol{\vartheta}_r,\ \boldsymbol{\theta}_t=\boldsymbol{\vartheta}_t, \tag{61b}$$

$$[\boldsymbol{\vartheta}_r]_n^2+[\boldsymbol{\vartheta}_t]_n^2=1,\ 1\le n\le N. \tag{61c}$$

With the method of Lagrange multipliers, the corresponding augmented Lagrangian can be formulated as

$$\underset{\boldsymbol{\theta}_r,\boldsymbol{\theta}_t,\boldsymbol{\vartheta}_r,\boldsymbol{\vartheta}_t}{\text{maximize}}\ \boldsymbol{\theta}_r^H\mathbf{Q}\boldsymbol{\theta}_r+2\mathcal{R}\left(\mathbf{q}^H\boldsymbol{\theta}_r\right)-\frac{\rho}{2}||\boldsymbol{\theta}_r-\boldsymbol{\vartheta}_r+\boldsymbol{\lambda}_{\boldsymbol{\theta}_r}||_2^2-\frac{\rho}{2}||\boldsymbol{\theta}_t-\boldsymbol{\vartheta}_t+\boldsymbol{\lambda}_{\boldsymbol{\theta}_t}||_2^2 \tag{62a}$$

$$\text{s.t. } (45b),(45c),\ [\boldsymbol{\vartheta}_r]_n^2+[\boldsymbol{\vartheta}_t]_n^2=1,\ 1\le n\le N, \tag{62b}$$

where the penalty $\rho>0$, $\boldsymbol{\lambda}_{\boldsymbol{\theta}_r}$ and $\boldsymbol{\lambda}_{\boldsymbol{\theta}_t}$ are dual variables associated with equality constraints in (61b). Then, we perform the optimization of $(\boldsymbol{\theta}_t,\boldsymbol{\theta}_r)$ and $(\boldsymbol{\vartheta}_t,\boldsymbol{\vartheta}_r)$ alternately, where the optimization of $(\boldsymbol{\theta}_t,\boldsymbol{\theta}_r)$ can be performed by employing MM.

APPENDIX B
PROOF OF THEOREM 1

We follow [68, Theorem 4] to show that the solution of problem (26) converges to the optimal solution of problem (21). Assuming that $\hat{\mathbf{s}}_\rho^*$ and $\tilde{\mathbf{s}}^*$ are the optimal solutions of problem (26) and problem (21), respectively, we have

$$\left(\hat{\mathbf{s}}_\rho^*\right)^T\hat{\mathbf{B}}\hat{\mathbf{s}}_\rho^*-\frac{\rho}{2}\Delta\left(\hat{\mathbf{s}}_\rho^*\right)\ge\left(\tilde{\mathbf{s}}^*\right)^T\hat{\mathbf{B}}\tilde{\mathbf{s}}^*-\frac{\rho}{2}\Delta\left(\tilde{\mathbf{s}}^*\right)\overset{(a)}{=}\left(\tilde{\mathbf{s}}^*\right)^T\hat{\mathbf{B}}\tilde{\mathbf{s}}^*, \tag{63}$$

where step (a) is due to the fact that $\tilde{\mathbf{s}}^*$ is a feasible solution of problem (21). Accordingly, we have $\Delta\left(\hat{\mathbf{s}}_\rho^*\right)\le\frac{2\left(\left(\hat{\mathbf{s}}_\rho^*\right)^T\hat{\mathbf{B}}\hat{\mathbf{s}}_\rho^*-\left(\tilde{\mathbf{s}}^*\right)^T\hat{\mathbf{B}}\tilde{\mathbf{s}}^*\right)}{\rho}$. Denoting $\hat{\mathbf{s}}_{+\infty}^*$ as the solution of problem (26) with $\rho\to+\infty$, we have $\Delta\left(\hat{\mathbf{s}}_{+\infty}^*\right)\le\lim_{\rho\to+\infty}\frac{2\left(\left(\hat{\mathbf{s}}_\rho^*\right)^T\hat{\mathbf{B}}\hat{\mathbf{s}}_\rho^*-\left(\tilde{\mathbf{s}}^*\right)^T\hat{\mathbf{B}}\tilde{\mathbf{s}}^*\right)}{\rho}=0$, since the difference value of $\left(\hat{\mathbf{s}}_\rho^*\right)^T\hat{\mathbf{B}}\hat{\mathbf{s}}_\rho^*-\left(\tilde{\mathbf{s}}^*\right)^T\hat{\mathbf{B}}\tilde{\mathbf{s}}^*$ is finite. Considering that $\Delta\left(\hat{\mathbf{s}}_{+\infty}^*\right)\ge0$, we have $\Delta\left(\hat{\mathbf{s}}_{+\infty}^*\right)=0$ and $\hat{\mathbf{s}}_{+\infty}^*$ is also a feasible solution of problem (21). Therefore, we have $\left(\tilde{\mathbf{s}}^*\right)^T\hat{\mathbf{B}}\tilde{\mathbf{s}}^*\ge\left(\hat{\mathbf{s}}_{+\infty}^*\right)^T\hat{\mathbf{B}}\hat{\mathbf{s}}_{+\infty}^*$. Finally, from (63), we have $\left(\hat{\mathbf{s}}_{+\infty}^*\right)^T\hat{\mathbf{B}}\hat{\mathbf{s}}_{+\infty}^*=\left(\tilde{\mathbf{s}}^*\right)^T\hat{\mathbf{B}}\tilde{\mathbf{s}}^*$ and we can conclude that $\hat{\mathbf{s}}_{+\infty}^*$ is also an optimal solution of problem (21).

APPENDIX C
PROOF OF THEOREM 2

Problem (21) can be reformulated as follows

$$\underset{\hat{\mathbf{s}}}{\text{maximize}}\ \hat{\mathbf{s}}^T\hat{\mathbf{B}}\hat{\mathbf{s}} \tag{64a}$$

$$\text{s.t. } \tilde{c}_{l,k}^u\left(\hat{\mathbf{s}}^*\right)=0,\ \hat{c}_{l,k}^u\left(\hat{\mathbf{s}}^*\right)=0,\tilde{c}_{l,j}^e\left(\hat{\mathbf{s}}^*\right)=0,\ \hat{c}_{l,j}^e\left(\hat{\mathbf{s}}^*\right)=0,\ c\left(\hat{\mathbf{s}}^*\right)=0,l\in\mathcal{L},k\in\mathcal{K}_u,j\in\mathcal{K}_e,||\hat{\mathbf{s}}-\hat{\mathbf{s}}_0||_2\le\sqrt{\epsilon L}, \tag{64b}$$

whose KKT conditions are formulated as follows:

$$\nabla_{\hat{\mathbf{s}}^*}\mathcal{L}\left(\hat{\mathbf{s}}^*,\varpi,\tilde{\varpi}_{l,k}^u,\hat{\varpi}_{l,k}^u,\tilde{\varpi}_{l,j}^e,\hat{\varpi}_{l,j}^e,\breve{\lambda}\right)=\mathbf{0}, \tag{65}$$

$$\tilde{c}_{l,k}^u\left(\hat{\mathbf{s}}^*\right)=\hat{c}_{l,k}^u\left(\hat{\mathbf{s}}^*\right)=\tilde{c}_{l,k}^e\left(\hat{\mathbf{s}}^*\right)=\hat{c}_{l,k}^e\left(\hat{\mathbf{s}}^*\right)=c\left(\hat{\mathbf{s}}^*\right)=0, \tag{66}$$

$$||\hat{\mathbf{s}}-\hat{\mathbf{s}}_0||_2\le\sqrt{\epsilon L}, \tag{67}$$

$$\breve{\lambda}\left(||\hat{\mathbf{s}}-\hat{\mathbf{s}}_0||_2-\sqrt{\epsilon L}\right)=0, \tag{68}$$

where ϖ, $\tilde{\varpi}_{l,k}^u$, $\hat{\varpi}_{l,k}^u$, $\tilde{\varpi}_{l,j}^e$, and $\hat{\varpi}_{l,j}^e$ are the Lagrange multipliers of the equality constraints in (64b) and

$$\mathcal{L}\left(\hat{\mathbf{s}}^*,\varpi,\tilde{\varpi}_{l,k}^u,\hat{\varpi}_{l,k}^u,\tilde{\varpi}_{l,j}^e,\hat{\varpi}_{l,k}^e,\breve{\lambda}\right)=-\hat{\mathbf{s}}^T\hat{\mathbf{B}}\hat{\mathbf{s}}+\sum_{k,l}\hat{\varpi}_{l,k}^u\hat{c}_{l,k}^u\left(\hat{\mathbf{s}}^*\right)+\sum_{j,l}\tilde{\varpi}_{l,j}^e\tilde{c}_{l,j}^e\left(\hat{\mathbf{s}}^*\right)+\sum_{j,l}\hat{\varpi}_{l,j}^e\hat{c}_{l,j}^e\left(\hat{\mathbf{s}}^*\right)+\varpi c(\hat{\mathbf{s}}^*)+\sum_{k,l}\tilde{\varpi}_{l,k}^u\tilde{c}_{l,k}^u\left(\hat{\mathbf{s}}^*\right)+\breve{\lambda}\left(||\hat{\mathbf{s}}-\hat{\mathbf{s}}_0||_2-\sqrt{\epsilon L}\right). \tag{69}$$

In the following, we focus on proving that Algorithm 1 satisfies the KKT conditions of problem (64). The proof is similar to [62, Theorem 2], which is presented for completeness. Firstly, the equality constraints can be augmented to the objective function by employing the penalty method, i.e.,

$$\underset{\hat{\mathbf{s}},\tilde{y}_k^u,\hat{y}_k^u,\tilde{y}_k^e,\hat{y}_k^e}{\text{maximize}}\ \hat{\mathbf{s}}^T\hat{\mathbf{B}}\hat{\mathbf{s}}-\frac{\rho}{2}\sum_{k,l}\left(\left(\tilde{c}_{l,k}^u\left(\hat{\mathbf{s}}^*\right)\right)^2+\left(\hat{c}_{l,k}^u\left(\hat{\mathbf{s}}^*\right)\right)^2\right)-\frac{\rho}{2}c^2\left(\hat{\mathbf{s}}^*\right)-\frac{\rho}{2}\sum_{j,l}\left(\left(\tilde{c}_{l,j}^e\left(\hat{\mathbf{s}}^*\right)\right)^2+\left(\hat{c}_{l,j}^e\left(\hat{\mathbf{s}}^*\right)\right)^2\right) \tag{70a}$$

$$\text{s.t. } ||\hat{\mathbf{s}}-\hat{\mathbf{s}}_0||_2\le\sqrt{\epsilon L}. \tag{70b}$$

Obviously, problem (70) is same as problem (26). The Lagrangian of problem (70) is given by

$$\hat{\mathcal{L}}\left(\hat{\mathbf{s}},\breve{\beta}\right) \triangleq -\hat{\mathbf{s}}^{T}\hat{\mathbf{B}}\hat{\mathbf{s}}+\breve{\beta}\left(\left|\left|\hat{\mathbf{s}}-\hat{\mathbf{s}}_{0}\right|\right|_{2}-\sqrt{\epsilon L}\right)+\frac{\rho}{2}c^{2}\left(\hat{\mathbf{s}}^{*}\right) + \frac{\rho}{2}\sum_{j,l}\left(\left(\tilde{c}^{u}_{l,k}\left(\hat{\mathbf{s}}^{*}\right)\right)^{2}+\left(\hat{c}^{u}_{l,k}\left(\hat{\mathbf{s}}^{*}\right)\right)^{2}\right) + \frac{\rho}{2}\sum_{j,l}\left(\left(\tilde{c}^{e}_{l,j}\left(\hat{\mathbf{s}}^{*}\right)\right)^{2}+\left(\hat{c}^{e}_{l,j}\left(\hat{\mathbf{s}}^{*}\right)\right)^{2}\right), \tag{71}$$

where $\breve{\beta}$ is the Lagrange multiplier of constraint (70b). Then,

$$\nabla_{\hat{\mathbf{s}}}\hat{\mathcal{L}}\left(\hat{\mathbf{s}},\breve{\beta}\right)\triangleq\Upsilon\left(\mathbf{s},\breve{\beta}\right)=-2\hat{\mathbf{B}}\hat{\mathbf{s}}+2\breve{\beta}\left(\hat{\mathbf{s}}-\hat{\mathbf{s}}_{0}\right)+\rho c\left(\hat{\mathbf{s}}^{*}\right)\nabla_{\hat{\mathbf{s}}^{*}}c\left(\hat{\mathbf{s}}^{*}\right) + \rho\sum_{k,l}\left(\tilde{c}^{u}_{l,k}\left(\hat{\mathbf{s}}^{*}\right)\nabla_{\hat{\mathbf{s}}^{*}}\tilde{c}^{u}_{l,k}\left(\hat{\mathbf{s}}^{*}\right)+\hat{c}^{u}_{l,u}\left(\hat{\mathbf{s}}^{*}\right)\nabla_{\hat{\mathbf{s}}^{*}}\hat{c}^{u}_{l,k}\left(\hat{\mathbf{s}}^{*}\right)\right) + \rho\sum_{j,l}\left(\tilde{c}^{e}_{l,j}\left(\hat{\mathbf{s}}^{*}\right)\nabla_{\hat{\mathbf{s}}^{*}}\tilde{c}^{e}_{l,j}\left(\hat{\mathbf{s}}^{*}\right)+\hat{c}^{e}_{l,j}\left(\hat{\mathbf{s}}^{*}\right)\nabla_{\hat{\mathbf{s}}^{*}}\hat{c}^{e}_{l,j}\left(\hat{\mathbf{s}}^{*}\right)\right). \tag{72}$$

As $\lim_{\rho\to+\infty}\Upsilon\left(\mathbf{s},\breve{\beta}\right)\to 0$, inequality (73) at the top of the next page can be obtained by employing the inequality $||a||-||b||\leq||a+b||$. Since $\nabla\hat{c}^{u}_{l,k}\left(\hat{\mathbf{s}}^{*}\right)$, $\nabla\tilde{c}^{u}_{l,k}\left(\hat{\mathbf{s}}^{*}\right)$, $\nabla\hat{c}^{e}_{l,k}\left(\hat{\mathbf{s}}^{*}\right)$, $\nabla\tilde{c}^{e}_{l,k}\left(\hat{\mathbf{s}}^{*}\right)$, and $\nabla c\left(\hat{\mathbf{s}}^{*}\right)$ are linearly independent, we can conclude that $\hat{c}^{u}_{l,k}\left(\hat{\mathbf{s}}^{*}\right)=\tilde{c}^{u}_{l,k}\left(\hat{\mathbf{s}}^{*}\right)=\hat{c}^{e}_{l,k}\left(\hat{\mathbf{s}}^{*}\right)=\tilde{c}^{e}_{l,k}\left(\hat{\mathbf{s}}^{*}\right)=c\left(\hat{\mathbf{s}}^{*}\right)=0$ satisfying constraint (66).

Besides, if we set $\varpi=\lim_{\rho\to+\infty}\rho\nabla_{\hat{\mathbf{s}}^{*}}c\left(\hat{\mathbf{s}}^{*}\right)$, $\tilde{\varpi}^{u}_{l,k}=\lim_{\rho\to+\infty}\rho\nabla_{\hat{\mathbf{s}}^{*}}\tilde{c}^{u}_{l,k}\left(\hat{\mathbf{s}}^{*}\right)$, $\hat{\varpi}^{u}_{l,k}=\lim_{\rho\to+\infty}\nabla_{\hat{\mathbf{s}}^{*}}\hat{c}^{u}_{l,k}\left(\hat{\mathbf{s}}^{*}\right)$, $\tilde{\varpi}^{e}_{l,k}=\lim_{\rho\to+\infty}\rho\nabla_{\hat{\mathbf{s}}^{*}}\tilde{c}^{e}_{l,k}\left(\hat{\mathbf{s}}^{*}\right)$, and $\hat{\varpi}^{e}_{l,k}=\lim_{\rho\to+\infty}\rho\nabla_{\hat{\mathbf{s}}^{*}}\hat{c}^{e}_{l,k}\left(\hat{\mathbf{s}}^{*}\right)$, condition (65) holds since $\lim_{\rho\to+\infty}\Upsilon\left(\mathbf{s},\breve{\beta}\right)\to 0$. Moreover, both conditions (67) and (68) hold, if we set $\breve{\beta}=\breve{\lambda}$. Now, we can conclude that the solution of problem (70) satisfies the KKT conditions of problem (64).

Besides, we employ the majorization-minimization algorithm [69] to approximate problem (70) as a sequence of convex optimization problems, i.e., problem (29). Since our proposed Algorithm 1 satisfies the conditions stated in [69, Eqs (2) and (3)], we can conclude that the converged solution of Algorithm 1 also satisfies the KKT conditions of problem (64).

REFERENCES

[1] C. Wang, C.-C. Wang, Z. Li, D. W. K. Ng, and K.-K. Wong, "PHY security enhancement exploiting STAR-RIS for dual-functional radar-communication," in *Proc. IEEE Intern. Commun. Conf. Workshops (ICCW)*, Rome, Italy, 2023, pp. 1–6.

[2] A. Zhang, M. L. Rahman, X. Huang, Y. J. Guo, S. Chen, and R. W. Heath, "Perceptive mobile networks: Cellular networks with radio vision via joint communication and radar sensing," *IEEE Veh. Technol. Mag.*, vol. 16, no. 2, pp. 20–30, Jun. 2021.

[3] F. Liu, Y. Cui, C. Masouros, J. Xu, T. X. Han, Y. C. Eldar, and S. Buzzi, "Integrated sensing and communications: Toward dual-functional wireless networks for 6G and beyond," *IEEE J. Sel. Areas Commun.*, vol. 40, no. 6, pp. 1728–1767, Jun. 2022.

[4] R. M. Mealey, "A method for calculating error probabilities in a radar communication system," *IEEE Trans. Space Electron. Telemetry*, vol. 9, no. 2, pp. 37–42, Jun. 1963.

[5] J. A. Zhang, F. Liu, C. Masouros, R. W. Heath, Z. Feng, L. Zheng, and A. Petropulu, "An overview of signal processing techniques for joint communication and radar sensing," *IEEE J. Sel. Top. Signal Proces.*, vol. 15, no. 6, pp. 1295–1315, Nov. 2021.

[6] J. A. Zhang, M. L. Rahman, K. Wu, X. Huang, Y. J. Guo, S. Chen, and J. Yuan, "Enabling joint communication and radar sensing in mobile networks—a survey," *IEEE Commun. Surveys Tuts.*, vol. 24, no. 1, pp. 306–345, Oct. 2022.

[7] Z. Wei, F. Liu, C. Masouros, N. Su, and A. P. Petropulu, "Toward multi-functional 6G wireless networks: Integrating sensing, communication, and security," *IEEE Commun. Mag.*, vol. 60, no. 4, pp. 65–71, Apr. 2022.

[8] F. Liu, Y.-F. Liu, A. Li, C. Masouros, and Y. C. Eldar, "Cramér-Rao bound optimization for joint radar-communication beamforming," *IEEE Trans. Signal Process.*, vol. 70, pp. 240–253, Jan. 2022.

[9] C. Sturm and W. Wiesbeck, "Waveform design and signal processing aspects for fusion of wireless communications and radar sensing," *Proc. IEEE*, vol. 99, no. 7, pp. 1236–1259, Jul. 2011.

[10] Y. Gu, L. Zhang, Y. Zhou, and Q. Zhang, "Embedding communication symbols into radar waveform with orthogonal FM scheme," *IEEE Sens. J.*, vol. 18, no. 21, pp. 8709–8719, Nov. 2018.

[11] R. Liu, M. Li, Q. Liu, and A. L. Swindlehurst, "Dual-functional radar-communication waveform design: A symbol-level precoding approach," *IEEE J. Sel. Top. Signal Proces.*, vol. 15, no. 6, pp. 1316–1331, Nov. 2021.

[12] X. Liu, T. Huang, N. Shlezinger, Y. Liu, J. Zhou, and Y. C. Eldar, "Joint transmit beamforming for multiuser MIMO communications and MIMO radar," *IEEE Trans. Signal Process.*, vol. 68, pp. 3929–3944, Jun. 2020.

[13] C. Wang, Z. Li, H. Zhang, D. W. K. Ng, and N. Al-Dhahir, "Achieving covertness and security in broadcast channels with finite blocklength," *IEEE Trans. Wireless Commun.*, vol. 21, no. 9, pp. 7624–7640, Sept. 2022.

[14] L. Chen, Z. Wang, Y. Du, Y. Chen, and F. R. Yu, "Generalized transceiver beamforming for DFRC with MIMO radar and MU-MIMO communication," *IEEE J. Sel. Areas Commun.*, vol. 40, no. 6, pp. 1795–1808, Jun. 2022.

[15] X. He and L. Huang, "Joint MIMO communication and MIMO radar under different practical waveform constraints," *IEEE Trans. Veh. Technol.*, vol. 69, no. 12, pp. 16 342–16 347, Dec. 2020.

[16] C. Xu, B. Clerckx, S. Chen, Y. Mao, and J. Zhang, "Rate-splitting multiple access for multi-antenna joint radar and communications," *IEEE J. Sel. Top. Signal Proces.*, vol. 15, no. 6, pp. 1332–1347, Nov. 2021.

[17] X. Mu, Y. Liu, L. Guo, J. Lin, and L. Hanzo, "NOMA-aided joint radar and multicast-unicast communication systems," *IEEE J. Sel. Areas Commun.*, vol. 40, no. 6, pp. 1978–1992, Jun. 2022.

[18] R. Liu, M. Li, Q. Liu, and A. L. Swindlehurst, "Joint waveform and filter designs for STAP-SLP-based MIMO-DFRC systems," *IEEE J. Sel. Areas Commun.*, vol. 40, no. 6, pp. 1918–1931, Jun. 2022.

[19] Q. Wu, S. Zhang, B. Zheng, C. You, and R. Zhang, "Intelligent reflecting surface-aided wireless communications: A tutorial," *IEEE Trans. Commun.*, vol. 69, no. 5, pp. 3313–3351, May. 2021.

[20] C. Wang, Z. Li, T.-X. Zheng, D. W. K. Ng, and N. Al-Dhahir, "Intelligent reflecting surface-aided secure broadcasting in millimeter wave symbiotic radio networks," *IEEE Trans. Veh. Tech.*, vol. 70, no. 10, pp. 11 050–11 055, Oct. 2021.

[21] S. Hu, Z. Wei, Y. Cai, C. Liu, D. W. K. Ng, and J. Yuan, "Robust and secure sum-rate maximization for multiuser MISO downlink systems with self-sustainable IRS," *IEEE Trans. Commun.*, vol. 69, no. 10, pp. 7032–7049, Oct. 2021.

[22] F. Wang, H. Li, and J. Fang, "Joint active and passive beamforming for IRS-assisted radar," *IEEE Signal Process. Lett.*, vol. 29, pp. 349–353, Dec. 2021.

[23] X. Wang, Z. Fei, Z. Zheng, and J. Guo, "Joint waveform design and passive beamforming for RIS-assisted dual-functional radar-communication system," *IEEE Trans. Veh. Technol.*, vol. 70, no. 5, pp. 5131–5136, May 2021.

[24] R. Liu, M. Li, Y. Liu, Q. Wu, and Q. Liu, "Joint transmit waveform and passive beamforming design for RIS-aided DFRC systems," *IEEE J. Sel. Topics Signal Process.*, vol. 16, no. 5, pp. 995–1010, May. 2022.

[25] N. Huang, T. Wang, Y. Wu, Q. Wu, and T. Q. S. Quek, "Integrated sensing and communication assisted mobile edge computing: An energy-efficient design via intelligent reflecting surface," *IEEE Wireless Commun. Lett.*, vol. 11, no. 10, pp. 2085–2089, Oct. 2022.

[26] M. Hua, Q. Wu, W. Chen, O. A. Dobre, and A. L. Swindlehurst, "Secure intelligent reflecting surface aided integrated sensing and communication," *arXiv preprint arXiv:2207.09095*, pp. 1–13, Jul. 2022.

[27] H. Du, J. Kang, D. Niyato, J. Zhang, and D. I. Kim, "Reconfigurable intelligent surface-aided joint radar and covert communications: Fundamentals, optimization, and challenges," *IEEE Veh. Technol. Mag.*, vol. 17, no. 3, pp. 54–64, Sept. 2022.

$$\left\| c\left(\hat{\mathbf{s}}^*\right) \nabla_{\hat{\mathbf{s}}^*} c\left(\hat{\mathbf{s}}^*\right) + \sum_{k,l} \left(\tilde{c}_{l,k}^{u}\left(\hat{\mathbf{s}}^*\right) \nabla_{\hat{\mathbf{s}}^*} \tilde{c}_{l,k}^{u}\left(\hat{\mathbf{s}}^*\right) + \hat{c}_{l,u}^{u}\left(\hat{\mathbf{s}}^*\right) \nabla_{\hat{\mathbf{s}}^*} \hat{c}_{l,k}^{u}\left(\hat{\mathbf{s}}^*\right) \right) + \sum_{j,l} \left(\tilde{c}_{l,j}^{e}\left(\hat{\mathbf{s}}^*\right) \nabla_{\hat{\mathbf{s}}^*} \tilde{c}_{l,j}^{e}\left(\hat{\mathbf{s}}^*\right) + \hat{c}_{l,j}^{e}\left(\hat{\mathbf{s}}^*\right) \nabla_{\hat{\mathbf{s}}^*} \hat{c}_{l,j}^{e}\left(\hat{\mathbf{s}}^*\right) \right) \right\|$$
$$\leq \frac{1}{\rho} \left(\left\| \Upsilon\left(\mathbf{s}, \breve{\beta}\right) \right\|_2 + \left\| 2\hat{\mathbf{B}}\hat{\mathbf{s}} - 2\hat{\mathbf{B}}\hat{\mathbf{s}} \right\|_2 \right) \overset{\rho \to +\infty}{\longrightarrow} 0. \tag{73}$$

[28] C. Wang, Z. Li, J. Shi, and D. W. K. Ng, "Intelligent reflecting surface-assisted multi-antenna covert communications: Joint active and passive beamforming optimization," *IEEE Trans. Commun.*, vol. 69, no. 6, pp. 3984–4000, Jun. 2021.

[29] J. Xu, Y. Liu, X. Mu, R. Schober, and H. V. Poor, "STAR-RISs: A correlated T & R phase-shift model and practical phase-shift configuration strategies," *IEEE J. Sel. Top. Signal Process.*, vol. 16, no. 5, pp. 1097–1111, Sept. 2022.

[30] X. Mu, Y. Liu, L. Guo, J. Lin, and R. Schober, "Simultaneously transmitting and reflecting (STAR) RIS aided wireless communications," *IEEE Trans. Wireless Commun.*, vol. 21, no. 5, pp. 3083–3098, May 2022.

[31] J. Xu, Y. Liu, X. Mu, and O. A. Dobre, "STAR-RISs: Simultaneous transmitting and reflecting reconfigurable intelligent surfaces," *IEEE Comm. Lett.*, vol. 25, no. 9, pp. 3134–3138, Sept. 2021.

[32] Y. Liu, X. Mu, J. Xu, R. Schober, Y. Hao, H. V. Poor, and L. Hanzo, "STAR: Simultaneous transmission and reflection for 360° coverage by intelligent surfaces," *IEEE Wireless Commun.*, vol. 28, no. 6, pp. 102–109, Dec. 2021.

[33] J. Zuo, Y. Liu, Z. Ding, L. Song, and H. Vincent Poor, "Joint design for simultaneously transmitting and reflecting (STAR) RIS assisted NOMA systems," *IEEE Trans. Wireless Commun.*, vol. 22, no. 1, pp. 611–626, Jan. 2023.

[34] N. DOCOMO, *Docomo Conducts World's First Successful Trial of Transparent Dynamic Metasurface*. [Online]. Available: https://www.nttdocomo.co.jp/english/info/mediacenter/pr/2020/0117_00.html,2020

[35] X. Yue, J. Xie, Y. Liu, Z. Han, R. Liu, and Z. Ding, "Simultaneously transmitting and reflecting reconfigurable intelligent surface assisted NOMA networks," *IEEE Trans. Wireless Commun.*, vol. 22, no. 1, pp. 189–204, Jan. 2023.

[36] Z. Wang, X. Mu, and Y. Liu, "STARS enabled integrated sensing and communications," *IEEE Tran. Wireless Commun.*, pp. 1–16, to be published, 2023.

[37] N. Su, F. Liu, and C. Masouros, "Secure radar-communication systems with malicious targets: Integrating radar, communications and jamming functionalities," *IEEE Trans. Wireless Commun.*, vol. 20, no. 1, pp. 83–95, Jan. 2021.

[38] N. Su, F. Liu, Z. Wei, Y.-F. Liu, and C. Masouros, "Secure dual-functional radar-communication transmission: Exploiting interference for resilience against target eavesdropping," *IEEE Trans. Wireless Commun.*, vol. 21, no. 9, pp. 7238–7252, Sept. 2022.

[39] H. Xu, T. Yang, K.-K. Wong, and G. Caire, "Achievable regions and precoder designs for the multiple access wiretap channels with confidential and open messages," *IEEE J. Sel. Areas Commun.*, vol. 40, no. 5, pp. 1407–1427, May 2022.

[40] P. Liu, Y. Li, W. Cheng, X. Gao, and X. Huang, "Intelligent reflecting surface aided NOMA for millimeter-wave Massive MIMO with lens antenna array," *IEEE Trans. Veh. Tech.*, vol. 70, no. 5, pp. 4419–4434, May 2021.

[41] S. Noh, H. Yu, and Y. Sung, "Training signal design for sparse channel estimation in intelligent reflecting surface-assisted millimeter-wave communication," *IEEE Trans. Wireless Commun.*, vol. 21, no. 4, pp. 2399–2413, Apr. 2022.

[42] W. Wang and W. Zhang, "Intelligent reflecting surface configurations for smart radio using deep reinforcement learning," *IEEE J. Select. Areas Commun.*, vol. 40, no. 8, pp. 2335–2346, Aug. 2022.

[43] Z. Cheng, Z. He, and B. Liao, "Hybrid beamforming for multi-carrier dual-function radar-communication system," *IEEE Trans. Cogn. Commun. Netw.*, vol. 7, no. 3, pp. 1002–1015, Mar. 2021.

[44] X. Liu, T. Huang, and Y. Liu, "Transmit design for joint MIMO radar and multiuser communications with transmit covariance constraint," *IEEE J. Sel. Areas Commun.*, vol. 40, no. 6, pp. 1932–1950, Mar. 2022.

[45] P. Stoica, J. Li, and Y. Xie, "On probing signal design for MIMO radar," *IEEE Trans. Signal Process.*, vol. 55, no. 8, pp. 4151–4161, Aug. 2007.

[46] G. Cui, H. Li, and M. Rangaswamy, "MIMO radar waveform design with constant modulus and similarity constraints," *IEEE Trans. Signal Process.*, vol. 62, no. 2, pp. 343–353, Jan. 2014.

[47] Z. Cheng, C. Han, B. Liao, Z. He, and J. Li, "Communication-aware waveform design for MIMO radar with good transmit beampattern," *IEEE Trans. Signal Process.*, vol. 66, no. 21, pp. 5549–5562, Nov. 2018.

[48] X. Yu, D. Xu, Y. Sun, D. W. K. Ng, and R. Schober, "Robust and secure wireless communications via intelligent reflecting surfaces," *IEEE J. Sel. Areas Commun.*, vol. 38, no. 11, pp. 2637–2652, Nov. 2020.

[49] W. Wang and W. Zhang, "Intelligent reflecting surface configurations for smart radio using deep reinforcement learning," *IEEE J. Sel. Areas Commun.*, vol. 40, no. 8, pp. 2335–2346, Aug. 2022.

[50] X. Zhang, *Matrix Analysis and Applications*. Second Edition. Beijing, China: Tsinghua University Press, 2013.

[51] R. Liu, M. Li, Q. Liu, and A. L. Swindlehurst, "Secure symbol-level precoding in MU-MISO wiretap systems," *IEEE Trans. Inf. Forensics Security*, vol. 15, pp. 3359–3373, Apr. 2020.

[52] A. Li, C. Masouros, B. Vucetic, Y. Li, and A. L. Swindlehurst, "Interference exploitation precoding for multi-level modulations: Closed-form solutions," *IEEE Trans. Commun.*, vol. 69, no. 1, pp. 291–308, Jan. 2021.

[53] W. Zhang, N. Zhao, S. Zhang, and F. R. Yu, "Intelligent reflecting surface enabled sensing: Cramér-rao lower bound optimization," *arXiv preprint arXiv:2204.11071*, 2022.

[54] M. R. A. Khandaker, C. Masouros, and K.-K. Wong, "Constructive interference based secure precoding: A new dimension in physical layer security," *IEEE Trans. Inf. Forensics Security*, vol. 13, no. 9, pp. 2256–2268, Sept. 2018.

[55] Y. Fan, R. Yao, A. Li, X. Liao, and V. C. M. Leung, "Robust deception scheme for secure interference exploitation under PSK modulations," *IEEE Trans. Commun.*, vol. 69, no. 8, pp. 5425–5440, Aug. 2021.

[56] Z. Wang, Y. Liu, X. Mu, Z. Ding, and O. A. Dobre, "NOMA empowered integrated sensing and communication," *IEEE Commun. Lett.*, vol. 26, no. 3, pp. 677–681, Mar. 2022.

[57] K. Zhong, J. Hu, C. Pan, X. Yu, and X. Li, "MIMO radar beampattern design based on manifold optimization method," *IEEE Commun. Lett.*, vol. 26, no. 5, pp. 1086–1090, May 2022.

[58] Y. Wu, D. Xu, D. W. K. Ng, R. Schober, and W. Gerstacker, "Globally optimal resource allocation design for IRS-assisted multiuser networks with discrete phase shifts," *arXiv preprint arXiv: 2302.12664*, pp. 1–6, Feb. 2023.

[59] A. Nemirovski and A. Ben Tal, *Lectures on Modern Convex Optimization. Analysis, Algorithms and Engineering Applications*. Philadelphia, USA: Society for Industrial and Applied Mathematics, 2001.

[60] R. Courant, "Variational methods for the solution of problems of equilibrium and vibrations," *Bull New Ser Am Math Soc*, vol. 49, pp. 1–23, 1943.

[61] E. C. Chi, H. Zhou, and K. Lange, "Distance majorization and its applications," *Math. Program*, vol. 146, pp. 409–436, Jun. 2014.

[62] C. Wang, Z. Li, N. Al-Dhahir, K. J. Kim, and K.-K. Wong, "QoS-aware precoder optimization for radar sensing and multiuser communications under per-antenna power constraints," *IEEE Trans. Signal Process.*, vol. 71, pp. 2235 – 2250, May 2023.

[63] K. Lange, *MM Optimization Algorithms*. Philadelphia, PA: Society for Industrial and Applied Mathematics, 2016. [Online]. Available: https://epubs.siam.org/doi/abs/10.1137/1.9781611974409

[64] S. Boyd and L. Vandenberghe, *Convex Optimization*. Cambridge, U.K.: Cambridge University Press, 2004.

[65] J. Nocedal and S. J. Wright, *Numerical Optimization*. 2nd ed. New York, NY, USA: Springer Science & Business Media, 2006.

[66] K. L. Keys, H. Zhou, and K. Lange, "Proximal distance algorithms: Theory and practice," *J. Mach. Learn. Res.*, vol. 20, pp. 1–38, 2019.

[67] A. Hjϕrungnes, *Complex-Valued Matrix Derivatives With Applications in Signal Processing and Communications*. New York, USA: Cambridge University Press, 2011.

[68] C. Wang, Z. Li, and D. W. K. Ng, "Covert rate optimization of millimeter wave full-duplex communications," *IEEE Trans. Wireless Commun.*, vol. 21, no. 5, pp. 2844–2861, May. 2022.

[69] Y. Sun, P. Babu, and D. P. Palomar, "Majorization-minimization algorithms in signal processing, communications, and machine learning," *IEEE Trans. Signal Process.*, vol. 65, no. 3, pp. 794–816, Feb. 2017.